Sinkholes in hypogene versus epigene karst systems, illustrated with the hypogene gypsum karst of the Sant Miquel de Campmajor Valley, NE Spain

Francisco Gutiérrez, Ivan Fabregat, Carles Roqué, Domingo Carbonel, Mario Zarroca, Rogelio Linares, Yoseph Yechieli, Ángel García-Arnay, Jorge Sevil

PII:	S0169-555X(18)30485-9
DOI:	https://doi.org/10.1016/j.geomorph.2018.12.003
Reference:	GEOMOR 6602
To appear in:	*Geomorphology*
Received date:	24 October 2018
Revised date:	6 December 2018
Accepted date:	7 December 2018

Please cite this article as: Francisco Gutiérrez, Ivan Fabregat, Carles Roqué, Domingo Carbonel, Mario Zarroca, Rogelio Linares, Yoseph Yechieli, Ángel García-Arnay, Jorge Sevil , Sinkholes in hypogene versus epigene karst systems, illustrated with the hypogene gypsum karst of the Sant Miquel de Campmajor Valley, NE Spain. Geomor (2018), https://doi.org/10.1016/j.geomorph.2018.12.003

Sinkholes in hypogene versus epigene karst systems, illustrated with the hypogene gypsum karst of the Sant Miquel de Campmajor Valley, NE Spain

Francisco Gutiérrez [a*], Ivan Fabregat [a], Carles Roqué [b], Domingo Carbonel [a], Mario Zarroca [c], Rogelio Linares [c], Yoseph Yechieli [d e], Ángel García-Arnay [a], Jorge Sevil [a]

[a] Departamento de Ciencias de la Tierra; Universidad de Zaragoza; C/. Pedro Cerbuna 12; 50009 Zaragoza; Spain; Phone: 34 976 761090

[b] Àrea de Geodinàmica Externa i Geomorfologia; Universitat de Girona; Campus Montilivi; E-17003 Girona; Spain

[c] Departamento de Geología; Universidad Autónoma de Barcelona; E-08193 Barcelona; Spain

[d] Geological Survey of Israel; 30 Malkhei Israel St.; Jerusalem 95501; Israel

[e] Zuckerberg Institute for Water Research; Ben-Gurion University; Sede Boqer Campus; 8499000; Israel

* Corresponding author Tel: +34 976 761090; Fax: +34 976 761106

E-mail address: fgutier@unizar.es (F. Gutiérrez)

Abstract

The Garrotxa-Banyoles artesian aquifer system in NE Spain includes zones with epigene and hypogene evaporite karst and sinkhole development. The sinkhole fields related to hypogene evaporite dissolution are associated with the discharge zones of the aquifer, where groundwater from a confined limestone rises traversing an overlying gypsum formation capped by thick marls. This work analyses the sinkhole field developed in the Sant Miquel de Campmajor Valley (SMCV), a discharge area of the aquifer, where a cartographic inventory including 94 sinkholes has been produced. Sinkholes in this hypogene gypsum karst are mainly large caprock-collapse sinkholes rooted in deep-seated cavities generated by interstratal hypogene karstification, as corroborated by an electrical resistivity imaging (ERI) survey. They show a non-clustered distribution within the sinkhole field and the variations in size and density across the area are mainly controlled by the thickness of the marl caprock. The magnitude and frequency relationships of the sinkholes can be modelled with a high goodness of fit with a log-normal function, like in other regions of the world. However, in this deep-seated hypogene system the depressions show much larger dimensions.

Potential differences between the sinkholes developed in hypogene and epigene karst environments are discussed, including their distribution with respect to the groundwater flow system, their spatial patterns and dimensions.

Key words

Interstratal karst, subsidence hazard, magnitude-frequency, electrical resistivity imaging (ERI)

1. Introduction

Bedrock-collapse sinkholes and caprock-collapse sinkholes in karst environments are the geomorphic expression of breakdown processes acting in the roof of significant cavities (e.g., Waltham et al., 2015). The formation of other sinkhole types such as sagging sinkholes and cover-collapse sinkholes do not necessarily require the presence of significant solutional voids in the subsurface (Gutiérrez et al., 2008, 2016). Sagging sinkholes may be related to the progressive dissolution of soluble rock, most commonly evaporites, and the concomitant passive bending of the overlying material. Cover-collapse sinkholes may result from the internal erosion of unconsolidated surficial deposits through solutionally enlarged discontinuities of limited size (i.e. grikes) in the epikarst. Two main karst systems are differentiated: epigene (or epigenetic) and hypogene (or hypogenic). Epigene systems are characterised by dominant downward groundwater flow from an overlying or adjacent recharge area. Caves are hydrologically and genetically linked to the landscape and typically display a branchwork or dendritic pattern, converging towards a main trunk channel connected to a spring. Epigene caves tend to expand downwards through the formation of progressively deeper water-table-controlled subhorizontal passages and vadose shafts (Palmer, 2007). Hypogene systems have been defined considering two different concepts: geochemical (i.e., source of aggressiveness) and hydrogeological (i.e., groundwater flow) (Dublyansky, 2014). According to Palmer (2007), in hypogene systems, karstification and cave development is mainly related to solutional aggressiveness generated at or below the water table, in contrast with epigene systems in which the aggressiveness is sourced at or near the land surface (e.g., soil CO_2). Potential deep sources of aggressiveness may include: (1) rising igneous fluids with acidic gases (CO_2, H_2S); (2) incorporation of H_2S (e.g., derived from sulphate reduction) that transforms into sulphuric acid by oxidation at or near the water table; (3) mixing of deep and shallow waters; (4) renewed aggressiveness of rising thermal waters by cooling; (5) mixing of waters with contrasting chemistry (e.g., seacoast mixing zones). Ford (2006) and Klimchouk (2007), using a hydrogeological approach, relate hypogene systems to karstification and cave-forming zones recharged from below and characterised by rising cross-formational flows, mainly under confined conditions. These caves tend to expand upwards throughout their evolution (e.g., Rehrl et al., 2008) and are less accessible that epigene caves.

The recent incorporation of the hypogene concept to the classical karst paradigms has entailed a great stimulus for the speleogenetic studies. Hypogene caves have received special attention in the last few years (e.g., Klimchouk et al., 2017). Sinkhole studies are also growing very rapidly largely due to their practical implications and increasing associated hazards and impacts (e.g., Gutiérrez, 2016). However, no attempts have been made to explore the possible differences between the sinkholes developed in epigene and hypogene karst systems, despite the clear cause-effect relationship that exists between caves and collapse sinkholes. The identification of potential features characteristic of sinkholes in the different karst systems could have practical implications for hazard assessment and risk management.

Regardless of the approach used to define hypogene karst systems, the different authors concur that hypogene caves have distinctive features (Klimchouk, 2007; Palmer, 2007; Audra et al., 2009), some of them with potential influence on the characteristics and patterns of the associated sinkholes: (1) Lack of relation to groundwater recharge and surface geomorphic features. (2) Common association with regional groundwater discharge areas. (3) Characteristic cave patterns include maze networks, spongework networks, as well as isolated and irregular chambers that may reach large dimensions (Frumkin and Fischhendler, 2005). The development of maze patterns requires adequate structural conditions and is favoured by the high discharge to flow length ratio of cross-formational flows of hypogene systems (i.e., the length of flow over which cave formation occurs is short) (Palmer, 2007). Moreover, the sluggish forced-flow of confined settings tends to enlarge all the discontinuities, rather than cause preferential karstification along favourable paths through positive flow-dissolution feedbacks (Klimchouk, 2007). (4) Hypogene dissolution tends to produce spatially restricted cave systems with lateral dead ends, covering areas of only a few square kilometres. (5) The density of solutional voids is much higher in hypogene caves. Klimchouk (2006) compared morphometric parameters of representative hypogene and epigene caves. He found that passage network density (cave length versus area of the cave field) and cave porosity (volume of cavities versus volume of the cave block) are one order of magnitude higher in hypogene caves. Similarly, average areal coverage (area occupied by passages in plan view versus area of cave field) is about five times higher in confined/epigene settings. (6) Typical internal landforms include rounded ceiling pockets and cupolas related to upward dissolution, frequently related to density convection flows.

This work analyses the hypogene gypsum karst and sinkholes of the Sant Miquel de Campmajor Valley (SMCV) in NE Spain, integrating geological, hydrological, hydrochemical and geomorphological data. The hypogene gypsum karst of the SMCV is contextualized within the regional Garrotxa-Banyoles aquifer system, which also includes sectors with epigene evaporite karst (Fluvia Valley), analysed in previous investigations (Gutiérrez et al., 2016; Fabregat et al., 2017). A detailed cartographic sinkhole inventory together with geophysical data are used to characterise the sinkholes of the SMCV, addressing aspects such as subsidence mechanisms, morphometric features, magnitude and frequency relationships and spatial-temporal distribution patterns. The results of the sinkhole analyses carried out in the hypogene and epigene evaporite karst sectors of the Garrotxa-Banyoles system, together with a literature review on sinkholes developed in hypogene gypsum karst settings worldwide, have served as the basis to preliminarily explore the potential differences between sinkholes developed in epigene and hypogene settings.

2. Geological setting

The study area corresponds to the N-S-oriented Sant Miquel de Campmajor Valley (SMCV), a tributary of the Ser River in NE Spain (Fig. 1). This is a region of complex geology related to two tectonic phases: (1) Alpine orogenic compressional phase (Late Cretaceous-Miocene), with the development of the Pyrenean orogene; (2) Neogene post-orogenic extensional phase (Late Miocene-present day), characterized by the development of down-to-the-east, NNW-SSE-trending normal faults superimposed on the previous contractional structures. These normal faults control Neogene grabens and Quaternary volcanic activity. Three main geological domains can be differentiated with influence on the hydrogeology of the karst aquifers underlying the SMCV (Fig. 1): the Pyrenees and the Ebro Cenozoic Basin, bounded by the E-W-trending and S-verging Vallfogona Thrust, and the Emporda Neogene Basin, controlled on its western margin by the Camos-Celra normal fault. The SMCV is located in the Ebro Cenozoic Basin, in the footwall of both the Vallfogona Thrust and the Camos-Celra Fault (Figs. 1, 2, and 3).

The region located N of the Vallfogona Thrust corresponds to the Cadí Unit of the eastern South Pyrenean Zone, comprising several major S-verging thrust structures (Teixell and Bur, 2000; Barnolas and Pujalte, 2004) (Figs. 2, 3A). The Cadí Unit can be subdivided into two main structural zones from N to S (Martínez et al., 1989; Gutiérrez et al., 2016) (Fig. 3A): (1) the Garrotxa structural complex; and (2) the Ripoll Synclinorium. The southern side of the Garrotxa structural complex is dominated by steeply dipping Mesozoic- to Eocene-age carbonate formations that form the Garrotxa carbonate massif, considered as the main recharge area for the karst aquifers in the region (e.g., Vidal-Pardal, 1957; Sanz, 1981, 1985; Linares et al., 2017) (Fig. 2 and 3A). The E-W-trending Ripoll Synclinorium consists of an Early-Middle Eocene succession around 2.5 km thick deposited in the former South-eastern Pyrenean foreland basin, and subsequently incorporated into the orogenic wedge through a piggy-back propagation sequence (Puigdefàbregas et al., 1986; Vergés et al., 1995; Carrillo et al., 2014). This foreland basin was characterized by an asymmetric geometry, comprising a deep trough associated with the orogenic wedge, grading into a shallow platform towards the southern forebulge. This configuration controlled significant facies and thickness changes within each chronostratigraphic unit (Puigdefàbregas et al., 1986; Carrillo et al., 2014), with impact of the current functioning of the karst aquifers. The lowermost sediments of the Ripoll Synclinorium, in fault contact with the limestones of the Garrotxa structural unit, are the Armancies Fm., an aquitard 100-200 m thick consisting of calcareous marls and shales, chronostratigraphically equivalent to the Early Eocene Girona limestone Fm. in the Ebro Basin (Fig. 3A).

In the Ebro Basin, south of the Vallfogona Thrust, where the SMCV is located (Fig. 1), the exposed Paleocene-Eocene sediments are affected by open E-W-striking folds related to the Pyrenean compression (Teixell and Muñoz, 2000) (Figs. 2, 3). Boreholes drilled up to the Paleozoic basement (metamorphic rocks) in the northern and southern sectors of the SMCV (Emporda-2, Campmajor-1), together with the available exposures, provide reliable direct information on the stratigraphic succession underlying the study area (Figs. 2, 3A). The following units can be differentiated in ascending order (Fig. 4):

(1) The Mediona Fm. (Late Paleocene); (2) The Orpí Fm. (Early Eocene); and (3) The Vilanova de Sau Fm. (Early Eocene) are detrital and carbonate units that do not play any significant role in the karstification of the evaporites underlying the SMCV.

(4) The Girona Fm. (Early Eocene) is a porous shallow marine arenaceous and bioclastic limestone 74-80 m thick in SMCV (Pallí, 1972; Mató et al., 1996; Puig et al., 1997a, b).

(5) The Beuda Fm. (Early-Middle Eocene) is the oldest unit exposed in the SMCV (Fig. 2). It consists of white and crudely bedded Ca-sulphates (gypsum/anhydrite) with interbedded bluish marls and limestones. This evaporitic body thickens towards the N, from 205 m in Campmajor-2 borehole to 293 m in Emporda-2 borehole (Fig. 3A). It was deposited in a relatively shallow platform-like basin (Carrillo et al., 2014). In the geological maps (e.g., Mató et al., 1996), this evaporitic succession is attributed to the Beuda Fm. However, Carrillo et al. (2014) based on borehole data differentiate four Ca-sulphate packages separated by carbonate-marl intervals, and ascribe the two lower ones to the Serrat Fm. In this work we use the term Beuda Gypsum to designate the thick evaporitic unit situated between the Girona and the Banyoles Fms. This is the karst formation responsible for the development of sinkholes in the area.

(6) The Banyoles Fm. (Middle Eocene) is an impermeable package more than 425 m thick mainly consisting of poorly stratified bluish grey marls. It locally includes a laterally discontinuous Ca-sulphate unit more than 10 m thick designated as the Besalu Gypsum (Carrillo et al., 2014), which crops out in the NE sector of the study area (Fig. 2).

(7) The Bracons and Bellmunt Fms. (Middle Eocene) is a thick detrital succession with a total thickness of around 600 m (Puigdefàbregas et al., 1986; Mató et al., 1996; Ramos et al., 2002).

(8) Post-Bracons (Late Eocene). The Bracons-Bellmunt succession is overlain by a ca. 500 m thick package of variegated sandstones with abundant bluish marls in the upper part (Puig et al., 1997a, b).

Extensional tectonics during the post-orogenic phase (Late Miocene to present-day) is recorded by a swarm of NNW-SSE-oriented normal faults superimposed to the Pyrenean contractional structures (Roqué et al., 2014). The master faults have a down-to-the-east throw, locally in excess of 1000 m, and control half-grabens progressively younger towards the west (footwall propagation sequence) (Saula et al., 1994). The

SMCV is located between the Llora and Cartella faults (Fig. 2). The Camos-Celra Fault, with a net displacement of ca. 1300 m (Saula et al., 1994), controls the western margin of the Emporda graben and acts as a major hydrogeological barrier for the karst aquifers (Fig. 3B).

3. Methodology

The hypogene gypsum karst of the SMCV and its sinkholes have been analysed integrating geological, geomorphological, hydrogeological, hydrochemical and geophysical data. A preliminary geomorphological and sinkhole map was produced through the interpretation of greyscale aerial photographs from 1957 and printed at an approximate scale of 1:32,000 (American Flight B). These images, despite their reduced scale, are particularly useful for the recognition of sinkholes due to limited anthropogenic disturbance and low vegetation cover at the time they were taken. Multitemporal images available in Google Earth Pro (2004, 04/2005, 06/2005, 2006, 2008, 2009, 2010, 2014 and 2015) and the viewer of the Institut Cartogràfic i Geològic de Catalunya (1946, 1957, 1986, 1991, 1993, 1995, 2002, 2003, and more recent) were used to refine the cartographic sinkhole inventory and constrain the timing of recent sinkhole events. Subsequently, a thorough field survey (9 journeys to cover 32 km^2) was conducted using 1:5,000 scale colour orthoimages to check the preliminarily mapped sinkholes and geomorphic features, including anomalies that could correspond to karst depressions. A template was used for the onsite characterization of each sinkhole, covering multiple aspects such as their geometry, morphometry, setting or degree of activity. Useful information on the spatial and temporal distribution of sinkholes was also obtained from local people, geotechnical reports, local publications (e.g., Fort, 1998; Abellán and Campos, 2008) and the City Hall of Sant Miquel de Campmajor. The spatial data were digitized with ArcGIS 10.5 (ESRI, 2017) using, for reference, colour orthoimages, a 1:10,000 scale topographic map, and a shaded relief model derived for a DEM (2 m of spatial resolution). These data layers were used to extract some morphometric parameters and perform several spatial distribution analyses.

Precipitation records and piezometric data from discharge zones were analysed in order to explore the hydraulic connection between different zones and the potential temporal relationship between wet and drought periods and sinkhole events. Piezometric data were facilitated by the Agència Catalana de l’Aigua (ACA) and downloaded from the interactive applications Global Aquifer Control (http://gac.cloudpp.net/aca) and Consulta de Datos de Control de la Calidad y Cantidad del Agua en el Medio (http://aca-web.gencat.cat/sdim21/). Precipitation records were downloaded from the Servei Meteorològic de Catalunya (www.meteo.cat).

The hydrochemical investigation was based on data available in previous reports (e.g., Sanz, 1985; Bach et al., 1986) and in the database of the local Water Authority (ACA), as well as the collection of samples in 10 points (springs, sinkhole ponds, Banyoles Lake) (Table 1, Fig. 5). The sampling points cover different sectors of the Garrotxa-Banyoles aquifer, from the recharge to the discharge zone, in order to explore the relationship between the carbonate and gypsum aquifers of this artesian system. Samples were collected in December 2016 and September 2017, in wet and dry seasons, respectively. At each point, two samples were collected for the determination of major ions and isotopes (^{18}O and ^{2}H), analysed in the hydrochemical laboratories of the Earth Sciences Department of the University of Zaragoza and the Geological Survey of Israel, respectively. Temperature, electrical conductivity and pH were measured in the field (see Acero et al., 2013 for details). Geochemical calculations (e.g., saturation indices) were performed with the PHREEQC code (Parkhust and Appelo, 2013) using the WATEQ4F thermodynamic database (Ball and Nordstrom, 2001) included in the PHREEQC package.

A 480 m long electrical resistivity imaging (ERI) section was acquired across a large caprock collapse sinkhole related to deep-seated gypsum dissolution. ERI is a direct-current method that images the distribution of the bulk resistivity in the subsurface using multielectrode systems (Griffiths and Baker, 1993; Loke et al., 2013). The survey was conducted in October 2017 with a Syscal Pro Swith System (IRIS Instruments) with 96 electrodes (5 m spacing) and a Dipole-Dipole (DDP) array. DDP was selected because it yields higher data saturation and higher sensitivity to lateral resistivity variations, expected to occur in a collapse sinkhole, in contrast to other arrays such as Wenner-Schlumberger (Dahlin and Zhou, 2004). The apparent resistivity data were inverted by the EarthImager2D inversion software (Advanced Geosciences, Inc.), based on the Occam's inversion (Constable et al., 1987; LaBrecque et al., 1996; Loke, 2011). The resistivity model was corrected to account for the ground topography by dump distortion using relative elevation data derived from a DEM (2 m horizontal resolution).

4. Hydrogeology

From the hydrogeological perspective, the SMCV is located within the Garrotxa-Banyoles karst aquifer system, which embraces portions of two different surface drainage basins; Fluvia and Ter (Terri) river catchments (Fig. 5). Here, we describe the main features of this artesian karst aquifer following the investigations carried out a few decades ago (Sanz and Trilla, 1982; Sanz et al., 1982; Bach et al., 1986), and incorporate some modifications to previous concepts. These novel ideas are based on the extensive knowledge gained recently on the stratigraphy and structure of the area (Martínez et al., 1997, 2000; Carrillo et al., 2014; Linares et al., 2017) and new hydrogeological and hydrochemical data.

The recharge area of the karst aquifer is located in the Garrotxa carbonate massif, with elevations above 1,100 m a.s.l. and situated north of the Ripoll Synclinorium and the Fluvia River valley (ca. 100 m a.s.l.) (Fig. 5). This groundwater input area, covering around 150 km^2 and with an average annual precipitation of 1100-1200 mm, consist of steeply dipping and karstified Eocene limestones of the Garrotxa structural complex. Here, most of the surface water infiltrates in bedrock outcrops and sinking streams (e.g., Llierca, Borro streams) (Vidal-Pardal, 1954). Recent geological knowledge suggests that the groundwater flows downwards through a stack of thrust sheets and duplexes dominated by limestone formations, traverses the Vallfogona Thrust, and incorporates into the Girona Fm. in the footwall (Fig. 5B). In the Ripoll Synclinorium and the Fluvia River valley, this deep carbonate aquifer is confined by a thick aquiclude comprising the salt-bearing Serrat evaporites and turbidites of the Vallfogona Fm (Martínez et al., 2000; Carrillo et al., 2014) (Fig. 3A). This confining package rapidly wedges out to the south due to the configuration of the Eocene foreland basin in which it was deposited; a deep trough associated with the orogenic wedge that grades into a shallow platform to the south (Puigdefàbregas et al., 1986; Carrillo et al., 2014). Further south, the Girona limestone is overlain directly by an evaporitic aquifer consisting of Ca-sulfate facies with marl intercalations of the Serrat and Beuda Fms (collectively referred to as Beuda Fm.). These associated carbonate and evaporitic aquifers are confined in most of the area by thick marls of the Banyoles Fm. (Figs. 3A, 5B).

Most probably, the NW-SE oriented and NE dipping Llora Fault defines the western boundary of the aquifer system (Fig. 3B). Its hectometre-scale throw is high enough to act as a hydrogeological barrier. The down-to-the-east Camos-Celra Fault controls the eastern boundary of the aquifer and the main discharge zone; i.e. Banyoles Lake (175 m a.s.l) (Fig. 5). It juxtaposes the carbonate and evaporitic aquifers (Girona and Beuda

Fms.) against impervious marls (Banyoles Fm.). During periods of high piezometric level, temporary springs located at higher elevations activate sequentially functioning as trop pleins or overflow springs: Bullidors in the SMCV (200 m a.s.l.) and Espolla (215 m a.s.l.), the latter also controlled by the Camos-Celra Fault (Fig. 5).

Previous works proposed the Fluvia River as an additional discharge area of the confined limestone aquifer. However, several arguments strongly suggest that this drainage is not connected with the Garrotxa-Banyoles aquifer system, which has its main discharge zone in a different surface catchment (Ter River) to the south: (1) recent geological data indicates that there is a thick aquiclude between the river and the Girona limestone; (2) in case there would be hydraulic connection, the main discharge zone of the aquifer would be the Fluvia River, which is the topographically lowest zone in the region; (3) the low-discharge springs with high concentration of dissolved evaporites located in the Fluvia River can be explained by local flows associated with the Beuda Gypsum, here hydraulically disconnected from the Girona limestone (Fig. 4).

The N-S oriented Banyoles Lake, located 5 km to the east of SMCV, is a 2 km long and 0.7 km wide compound sinkhole comprising multiple coalescing and nested collapse structures developed in the Banyoles marls (Canals et al., 1990; Brusi et al., 1992) (Fig. 5). This permanent lake, with a maximum depth of 132 m (Canals et al., 1990), is fed at different points in its bottom by artesian springs with an estimated average discharge of $12 \cdot 10^6$ m^3/y (IGME, 1986). The upward groundwater flow from the Girona Fm. traverses the Beuda Gypsum, causing its karstification and the development of caprock collapse sinkholes. A significant proportion of the lake water flows into the Terri River, a tributary of the Ter River. In the surroundings of Banyoles, wells as much as 220 m deep extract water from the Girona limestone. The groundwater in this lower confined aquifer (Girona Fm.) reaches pressures of 3.5 atm and has sulphate contents of around 300-350 mg/l (Bach et al., 1986). In contrast, the spring water at the lake bottom, after traversing the upper gypsum aquifer (Beuda Fm.), has sulphate concentrations typically higher than 1000 mg/l (Sanz and Trilla, 1980; Sanz, 1985; Bach et al., 1986). The spring water is saturated with respect to calcite, largely due to the common ion effect related to gypsum dissolution and the input calcium. This fault-controlled groundwater discharge area is characterised by long-sustained tufa deposition recorded by: (1) the >70 m thick Plio-Quaternary Incarcal-Usall Fm. that forms a 10x3 km structural platform on the footwall of the Camos-Celra Fault (Usall platform), perched 45 m above the Banyoles Lake (Julià, 1980); and (2) Pleistocene-Holocene tufas in the bottom the Banyoles Lake basin (Mató et al., 1996).

Canals et al. (1990), by means of high-resolution seismic reflection surveys conducted in Banyoles Lake, documented collapse structures, slumps and suspensates up to 44 m thick. The latter are deep zones of the lake associated with the subaqueous springs with a high concentration of suspended sediment related to upwelling groundwater flows. Bischoff et al. (1994) proposed that dedolomitization processes and the consequent decrease in the activity calcium contribute to enhance gypsum dissolution beneath Banyoles Lake. These authors also estimated that karstification by artesian waters creates around 9500 m^3 of subsurface voids per year beneath the lake basin. Several authors document historical collapse events in the Banyoles Lake basin. Sudden water level changes in the lake occurred in 1904, 1920, 1949 and 1984 were attributed to rapid subaqueous collapse events (Sanz, 1985; Brusi et al., 1987). Recent paleolimnological investigations identify evidence of collapses and mass movements in the stratigraphic record probably correlated with dry and low piezometric-level periods (Höbid et al., 2012; Morellón et al., 2014), and homogenite layers ascribed to fluidization processes induced by enhanced spring discharge and fluid overpressure (Serra et al., 2002, 2005; Soler et al., 2009; Morellón et al., 2014).

The Espolla temporary spring, with an average discharge of $5 \cdot 10^6$ m^3/y (IGME, 1986, 1990), is located in the Usall platform at 215 m a.s.l., 40 m above the Banyoles Lake. This spring, also controlled by the Camos-Celra Fault, only functions during periods of high piezometric level (overflow spring). Vidal-Pardal (1960), based on borehole data, documented large cavities in the Plio-Quaternary Usall-Incarcal calcareous tufas, attributable to collapse chimneys rooted in the Beuda Gypsum and penetrating the overlying Banyoles marls.

In the SMCV, the Bullidors temporary springs, at around 200 m a.s.l., are associated with an outcrop of the Beuda Gypsum and the Tort Stream. Here, springs may be perched several meters above the river bed and discharge may reach 2300 l/s (Sanz and Trilla, 1980). These can be considered as estavelles or reversing springs in a karst window, that function as overflow springs during periods of high piezometric level, feeding the Tort River (effluent stream), and as ponors when the piezometric level is below the topographic surface (influent stream). The groundwater in the Bullidors springs is characterised by high sulphate concentrations and electrical conductivity (1200-1250 mg/l, ~2500 μS/cm) and stable temperature (19-20°C) above the average ambient temperature (15°C). These springs cause significant hydrochemical degradation of the Tort Stream, typically with sulphate concentrations of 70 mg/l upstream of the Bullidors springs (Trilla et al., 1979; Bach et al., 1986).

Several tracers have been used to demonstrate the hydraulic connection between the Garrotxa Massif and the different springs (Banyoles Lake, Bullidors, Espolla), as well as to characterise some features of this complex artesian karst aquifer. Sanz et al. (1982) carried out systematic ^{18}O determinations from (1) infiltration water in the Llierca Stream; and (2) groundwater in the discharge areas of SMCV (Bullidors) and the Banyoles Lake Basin (artesian well that exploits the confined limestone aquifer at 220 m depth). They also sampled rainwater at different elevations to determine the rate at which $\delta^{18}O$ values decrease with elevation. The ^{18}O concentrations were very similar in the Garrotxa Massif and the spring areas, supporting their hydraulic connection. Moreover, the ^{18}O signature of the springs correlates with those of rainwater at 700-900 m elevation, demonstrating that most of the recharge occurs in the Garrotxa Massif. In a subsequent work, Sanz and Trilla (1982), by systematically determining and comparing tritium (^{3}H) concentrations in the rainwater at the Garrotxa Massif and in the main discharge areas (Bullidors and wells in Banyoles exploiting the limestone aquifer), estimated a residence time for the groundwater of 11-18 months.

As part of this investigation, the temporal variations of piezometric levels recorded in the SMCV and in the Espolla spring area have been plotted in Fig. 6 (data from the Agencia Catalana de l'Aigua). The piezometer in the SMCV measures the potentiometric level in the gypsum aquifer. In the Espolla spring area, there are three piezometers that measure the hydraulic head in the gypsum aquifer (Fontcoberta-3 and -2) and in the surficial tufaceous aquifer (Fontcoberta-1) (Linares et al., 2017). The relatively good correlation between the different records strongly support that the SMCV and the discharge areas located to the east (Espolla, Banyoles) are in hydraulic connection and form part of the same regional aquifer system. Some apparent mismatches may be attributed to gaps in the time series of the SMCV.

Two different types of gypsum karst can be differentiated within the Garrotxa-Banyoles hydrogeological system, determined by the different stratigraphic relationships between the gypsiferous sediments of the Beuda Fm. and the underlying carbonate aquifer of the Girona Fm. In the Fluvia Valley area, where both units are separated by a thick aquiclude (Serrat and Vallfogona Fms.), the gypsum karst has an epigene nature. Dissolution is caused by groundwater that is recharged from above (Gutiérrez et al., 2016), In contrast, in the SMCV, as well as in the Banyoles Lake basin and the Espolla spring area, the gypsum karst can be classified as hypogene in the sense of Ford (2006) and Klimchouk (2007), since most of the dissolving groundwater is derived from an underlying confined aquifer. This is a peculiar case in which a gypsiferous formation exhibit two different styles of karstification in a short distance, determined by the rapid wedging out and disappearance of an underlying impervious unit.

5. Hydrochemistry

Here we analyse chemical and isotopic data to test the hydrogeological model described above and gain insight into the hypogene karstification involved in the development of sinkholes. The analysed chemical information has been collected during this investigation (December 2016, September 2017) and obtained from available publications (Trilla et al., 1979; Sanz, 1985; Bach et al., 1986; IGME, 1990) and the database of the Agència Catalana de l'Aigua (Table 1). Different types of water can be differentiated according to their hydrochemistry and position within the hydrogeological system. The location of some of the sampling points is indicated in the generalised cross-section of the Garrotxa-Banyoles aquifer system (Fig. 5):

Points 1, 2, 3 and 4 represent surface and underground water in the recharge area (Garrotxa cabonate massif) that has interacted with carbonate rocks, showing very low SO_4 concentrations (<32 mg/l), Ca balanced by the HCO_3 (Ca/HCO_3 ratios ~1), and SO_4/HCO_3 ratios ≤ 0.6 (Table 1). Point 1, with lower concentrations, corresponds to surface water sampled in the Llierca Stream upstream of the main ponors. Points 2, 3 and 4 are karst springs saturated with respect to calcite and related to local groundwater flows in the limestone aquifer that has not been incorporated into the deep regional system.

Points 5 and 6 characterise groundwater from the carbonate aquifer in the discharge area (Banyoles Lake basin), that has not traversed the overlying gypsum package. The water was collected in artesian wells. These waters have sulphate concentrations (300-350 mg/l) around 10 times higher than those of the recharge area, but are still undersaturated with respect to gypsum. This increase in sulphate concentration may be related to some interaction with gypsum along the long flow path and to mixing in the well from the overlying gypsum aquifer, but the Ca/SO_4 ratios are well above 1 (Table 1).

Points 7, 8, 9 and 10 essentially represent spring waters in the discharge areas (SMCV and Banyoles Lake basin). Points 7 and 10 are springs and points 8 and 9 sinkhole lakes with different depths fed by bottom springs. Overall, these waters show HCO_3 concentrations similar to those of the deep carbonate aquifer in the discharge area (ca. 300 mg/l), but much higher sulphate contents (600-1450 mg/l). As illustrates Fig. 7, these waters, saturated with respect to gypsum, and with high Ca/HCO_3 and SO_4/HCO_3 ratios and Ca/SO_4 ratios close to one, constitute a markedly different hydrochemical group. These chemical features suggest that the water has been flowing through gypsum layers for enough time to reach saturation. Lower concentrations in point 9 (surface water in Banyoles Lake) can be attributed to the stratification of the water in the lake documented by Sanz (1985). Apparently, the obtained sample was taken from the upper water layer in this lake and therefore of lower concentration. These hydrochemical features strongly support the concept that the spring waters in SMCV and Banyoles Lake basin have flowed upwards from the Girona Limestone traversing the Beuda Gypsum, and causing its hypogene karstification.

Points 11, 12, 13, 14, located in different settings, essentially show a stoichiometric balance between Ca and HCO_3 and low SO_4 concentrations (<190 mg/l), indicating that they have not significantly interacted with gypsum units (i.e., Beuda Gypsum). These are most probably surface waters and local groundwater flows that have mainly interacted with the thick and extensively exposed Banyoles Fm., consisting of marls and minor interbedded gypsum beds. Points 11 and 12 correspond to two sinkholes ponds in the SMCV (Balca and Coromina) that do not seem to be hydraulically connected with the artesian regional flow.

Most of the ^{18}O and ^{2}H results of the waters sampled in December 2016 fall between the Global Meteoric Water Line (MWL) and the Local Meteoric Water Lines (LMWL). The samples from the Garrotxa Massif (samples 1-4) have more negative isotopic values, as expected due to their higher elevation, similar to what was found in previous studies (Sanz et al., 1982). In general, the similar isotopic values in groundwater in the whole area indicate that the main recharge is in the Garrotxa Massif. The somewhat less negative isotopic signature in some samples may imply that part of recharge is not at the high Garrotxa Massif but at lower altitudes. The specific location and proportion of this recharge is difficult to determine but the isotopic values imply some mixing of several sources of water. The samples from points 8, 9, 10 and 14 are close to the autumn LMWL of Vilanova et al. (2008), which is the period of highest recharge. This group of points, with the exception of point 14, are discharge waters from the regional artesian aquifer. The rest of samples occur near the annual LMWL. Only one sample (point 12) is significantly off the meteoric line, attributable to the effect of local evaporation. Such evaportation is more pronounced here probably due to low water flow rate (Fig. 8). Moreover, this is a relatively shallow sinkhole pond whose water body has a high surface/volume ratio.

6. Geomorphology and sinkhole analysis

6.1. Geomorphology of the SMCV

The SMCV is an erosional depression around 8 km long and 3-5 km wide with a N-S orientation perpendicular to the E-W trending folding structure. The bedrock is affected by a major E-W-striking anticline whose axis runs across the central sector of the valley (Fig. 3A). This is the area where the only outcrops of Beuda Gypsum occur in the valley, and the Quaternary alluvium is locally in direct contact with evaporitic bedrock (mantled karst) (Fig. 9). The contact between the Beuda Gypsum and the overlying Banyoles Marls plunges to the N and S, reaching depths of more than 200 m below the valley bottom according to borehole data (Figs. 3A). In the northern and southern sectors of the valley, where the level of erosion has not reached the top of the Beuda Gypsum, subsidence related to the karstification of this evaporitic formation affects to a thick caprock of Banyoles Marls (interstratal karst).

The topography of the valley is characterised by a flat floor, bounded by relatively steep slopes underlain by Banyoles Marls and the overlying Eocene detrital formations (Bracons and Bellmunt Fms.). The latter, more resistant to erosion, control the prominent water divides on the eastern and southern sides of the watershed. The valley is mainly drained by the axial Sant Miquel and Ritort creeks. Interestingly, the Upper Ritort Creek has captured part of the adjacent basin to the west through a saddle carved in the Banyoles Marls (Fig. 9). The temporary Bullidors springs are located in the junction area between the Sant Miquel and Ritort creeks, associated with the axial zone of the E-W anticline where the Beuda Gypsum crops out.

A total of three alluvial levels have been identified in the valley, including the floodplain (T1: + 20-31 m, T2: + 8-16 m, T3: + 2-7 m), and two pediment levels (P2 and P3) correlative to the two older terraces (Fig. 9). The oldest alluvial level only occurs in the northern sector, close to the junction with the Ser River. Terrace and pediment deposits are typically less than 5 m thick and mainly consist of fine-grained facies with interbedded gravel beds. Terrace deposits locally include tufa facies (Pallí and Trilla, 1979; Mató et al., 1996). The drainage in the upper and eastern sectors of the basin show broad flat-bottomed infilled valleys that grade to the gentler floodplain.

6.2. General features and genesis of the inventoried sinkholes

Previous cartographic works document a significant number of sinkholes in the SMCV (Pallí and Trilla, 1979; Mató et al., 1996). Information on the spatial and temporal distribution of sinkholes is also found in local publications. These pay special attention to historical collapse events and sinkhole ponds, due to their ecological value (e.g., Fort, 1998; Abellán and Campos, 2008; Abellán, 2010). In this work we have inventoried 94 sinkholes covering a total area of 0.69 km^2, yielding a density of 2.9 sinkholes/km^2 and a percentage area covered by sinkholes of 2.16%, considering the total surface of the SMCV (32 km^2) (Figs. 9, 10). These values rise to 14 sinkholes/km^2 and 10.3% considering a polygon (sinkhole field) that embraces all the mapped sinkholes (6.7 km^2). A striking feature of the sinkholes in the SMCV is the presence of numerous hectometre-scale depressions that chiefly occur in the non-alluviated slopes of the valley margin. The major axis of the bottom of the largest sinkhole, located just north of Falgons, reaches 309 m. The total volume of the inventoried sinkholes has been estimated at 6 hm^3, considering the area of the bottom of the depressions and their average depth. The two largest sinkholes, located north and south of Falgons, in the southwestern sector of the valley, account for 49% of the total volume. The aggregate volume can be considered as a minimum estimate of the relief generated by dissolution-induced subsidence, since the depth of the sinkholes has decreased by aggradation and the inventory is incomplete. The estimated value indicates a minimum average surface lowering by subsidence of 0.9 m in the polygon that embraces all the sinkholes.

The majority of the sinkholes in SMCV show scarped edges and circular or subcircular geometries in plan view (Fig. 10). The depressions can be classified according to their elongation ratio (R=major axis/minor axis; e.g., Basso et al., 2013) into circular (R=1; 36.6%); subcircular (1<R<1.2; 31.2%); elliptical (1.21<R<1.65; 29%); and elongated (R>1.66; 3.2%). Consistently, the sinkholes have an average circularity index of 0.963 (standard deviation of 0.06), given by the ratio between the area of the depressions and the area of a perfect circle with the same perimeter (e.g., Denizman, 2003; Brinkman et al., 2008). The sinkholes have been classified qualitatively into three morphological types, following the classical subdivision of Cvijic (1893) and adopted in numerous works (e.g., Kranjc, 2013; Gutiérrez et al., 2016); well-shaped (24.5%) funnel-shaped

(69.1%), and pan-shaped (6.4%). Some sinkholes have a more complex morphology due to the presence of nested depressions or the coalescence of adjacent dolines. The morphological features described above indicate that collapse is the dominant subsidence mechanism in the valley. Funnel-shaped depressions are essentially former well-shaped sinkholes with degraded margins. Moreover, following the genetic classification of sinkholes proposed by Gutiérrez et al. (2008) and Gutiérrez (2016) and based on our knowledge on the local geology, we estimate that more than 70% of the sinkholes correspond to caprock and cover collapse sinkholes or caprock collapse sinkholes. These are sinkholes related to the interstratal dissolution of Beuda Gypsum in areas where this formation is overlain by the Banyoles Marls (caprock), and locally also a thin veneer of alluvium (cover). Around 70% of the sinkholes occur on alluvial surfaces. Interestingly, some of the largest sinkholes occur in the northern and southern sectors of the valley, where the top of the Beuda Gypsum is situated at around 100-250 m depth. This fact reveals that the sinkholes are related to deep-seated hypogene dissolution in the confined Beuda Gypsum and the development of large collapse structures. For instance, the top of the Beuda Gypsum beneath the large caprock collapse sinkhole located in Falgons Creek is more than 200 m deep. Considering the area of the bottom of the sinkhole, we can estimate a minimum volume for the collapse structure of $9.2 \cdot 10^6$ m^3 (equivalent to a cube 210 m in edge).

6.3. Spatial distribution and controlling factors

The dominant circular to subcircular geometry of the sinkholes and the dispersion of the orientation of the major axes, illustrated in the rose diagram inset in Fig. 9, suggest limited structural control on the dissolution and subsidence processes in the SMCV. The rose diagram weakly indicates a preferred NE-SW orientation of the major axes of the sinkholes. North of Falgons there is a clear NW-SE alignment of large sinkholes. To the southwest of Can Coromina several sinkholes define a NNE-SSW lineament. These variable orientations do not coincide with the main structural grains of the region; E-W Alpine folding and NNW-SSE post-orogenic normal faulting.

Overall, the comparison of the distribution of the inventoried sinkholes with the different geomorphic and geological zones indicates the following main features (Fig. 11): (1) The density of sinkholes by number is higher in the central sector of the valley and along the valley bottom, showing some spatial association with channels (Fig. 9, 11A). (2) The largest sinkholes occur in the slopes underlain by Banyoles Marls of the valley margins and in the northern and southern sector of the valley (Fig. 11B). This spatial pattern is illustrated by two different types of sinkhole density maps generated with a Kernel function and a search radius of 650 m, which assess the number of sinkholes (centroids) and the area affected by sinkholes (percentage area within sinkholes) (Fig. 11). The latter implicitly weights the sinkholes according to their size. Six density classes were discretized through the natural break method. The higher spatial frequency of sinkholes in the central sector of the valley (axial zone of the anticline) and the larger size of the depressions in the northern and southern sectors is also illustrated in a graph that shows the number of sinkholes and their average size in E-W-oriented bands 1 km wide (Fig. 11C). The anomalous high frequency of sinkholes in the sloping margins of the valley is illustrated by the fact that around 50% of the sinkholes occur in areas with average slopes between 10° and 20°, estimated considering a 20 m buffer around each sinkhole (see Supplementary Data 1).

The geomorphological map shows that a significant proportion of sinkholes are associated with channels showing various types of interactions. Some sinkholes have intercepted channels acting as ponors (Can Coromina; Fig. 10B). Once the sinkholes are filled and the throughgoing flow is re-established, the channel sections show a clear decrease in their longitudinal gradient. Other sinkholes have controlled the path of channels, contributing to increase their sinuosity, such as the Ritort Creek (meaning tortuous). A graph of the cumulative frequency of sinkholes (centroids) versus the distance to the nearest channel indicates that 46% of the sinkholes are located at less than 50 m from the nearest channel (see Supplementary Data 2).

The relative spatial distribution of the inventoried sinkholes can be quantitatively analysed using the Nearest Neighbour Index (NNI; Clark and Evans, 1954). This index (NNI=La/Le) compares the average distance between nearest sinkholes in the study area (La) with the mean theoretical distance between nearest sinkholes (Le) in a field with random distribution and the same density (D). The theoretical distance Le is given by $1/2\sqrt{D}$. This index has been widely used in sinkhole analyses (Gutiérrez, 2016) to characterize the relative distribution of sinkholes since the seminal work by Williams (1972). A NNI equal to 2.15 indicates maximum dispersion with uniform hexagonal pattern, 1 perfect random distribution, and 0 maximum clustering (every sinkhole attached to another). A NNI of 1.3 has been computed, considering for the density calculation the polygon that embraces all the sinkholes. This value indicates that the sinkholes have an overall random distribution and a limited tendency to form clusters.

As shows the geomorphological map, the number of sinkhole clusters is very limited. The apparent spatial independence of the sinkholes is also illustrated by a cumulative frequency plot constructed with the distance of each sinkhole to the nearest neighbor (Fig. 12). This curve indicates the proportion of sinkholes in the inventory that occur at a distance to the nearest sinkhole equal or lower than a specific value. In the hypogene karst of SMCV, only 16% of the sinkholes occur at a distance of ≤50 m, in contract with the epigene karst of the Fluvia Valley, where percentage of sinkholes reaches 37% for the same distance (Gutiérrez et al., 2016).

6.4 Magnitude and temporal frequencies and hazard implications

Sinkhole-related subsidence has a limited impact in the SMCV, mainly due to the reduced exposure and the relatively low probability of occurrence of sinkholes, despite the large size of numerous depressions. To our knowledge, the main detrimental effects are related to loss of agricultural land, cracking in buildings (Sant Miquel) and severe leakage from a water retention pond. Moreover, in the 1950s, the construction of a 65 m high dam across the Ser River, that would create a reservoir with a capacity of 170 10^6 m^3 impounding a section of the Ser Valley and the lower reach of the SCMV, was dismissed due to potential water loss through sinkholes towards the Banyoles Lake (Vidal-Pardal, 1954). The assessment of the spatial and temporal frequencies of sinkholes of different sizes (hazard parameters) in this hypogene gypsum karst setting has both scientific and practical interest.

The frequency-size relationships of the inventoried sinkholes have been explored plotting the major axes of the depressions, ranging from 309 m to 2 m, and the cumulative frequency (Fig. 13). The empirical data, plotted on a graph with the major axial length in logarithmic scale, show a linear distribution that can be modelled by a log-normal function with a high goodness of fit (R^2=0.94) and covering around 2 orders of magnitude. The fit line has been plotted together with the empirical data and regressions obtained for sinkholes developed in other regions, all of them with coefficients of determination (R^2) above 0.92 (Gombert et al., 2015; Taheri et al., 2015; Gutiérrez and Lizaga, 2016; Gutiérrez et al., 2016). The scaling relationships of the sinkholes inventoried in different karst settings are discussed below. In the case of the SMCV, where sinkholes tend to reach larger dimensions, the regression function roughly estimates that the frequency of sinkholes with major axes equal or larger than 5 m, 10 m and 100 m are 0.99, 0.68 and 0.32, respectively. The deviation of the empirical data from the regression line corresponding to the small sinkholes (<10 m) may be related to the expected incompleteness of the inventory; depressions of reduced size are more difficult to detect. The largest inventoried sinkholes (>100 m) also show lower probabilities that those modelled by the regression function. This deviation may be partially related to mechanical thresholds (upper bound) determined by the size of the largest cavity span that may be developed in this stratigraphic context before its collapse.

Regarding the spatial distribution of sinkholes, it is interesting to explore whether the new sinkholes tend to occur in the proximity of the pre-existing sinkholes and assess the predictive utility of the latter. Some authors contend that sinkholes are the best predictors of future subsidence events (e.g., Magdalene and Alexander, 1995). Kemmerly (1982) hypothesized that the formation of a sinkhole (mother doline) creates favourable conditions for the generation of new sinkholes (daughter dolines) in its vicinity. These are generally the areas where sinkholes tend to cluster and offer the best possibilities for developing reliable spatial predictions (susceptibility models) based on cartographic sinkhole inventories. However, in some areas spatial analyses indicate that the occurrence of new sinkholes tends to be a random process independent of the distribution of pre-existing sinkholes (McConnell and Horn, 1972). For instance, Hyatt et al. (1999), in the mantled limestone karst of Albany, Georgia, USA, examined the spatial relationships between 311 new sinkholes triggered in July 1994 by flooding caused by tropical storm Alberto and 329 pre-existing sinkholes. They found through nearest neighbour analyses that the new sinkholes did not cluster near old sinkholes. In the case of SMCV, we have explored the relative spatial distribution between the 11 historical sinkholes of known age, dating back from 1872, and that of the pre-existing sinkholes. A cumulative frequency plot versus distance to the nearest pre-existing sinkhole shows limited spatial association between the old and new sinkholes (Fig. 12B**).** Only four sinkholes out of eleven occur at less than 60 m from the nearest pre-existing sinkhole and the distribution shows a rather diagonal pattern, rather than a steep line.

Regarding the spatial distribution of the 11 historical sinkholes, all of them occur associated with the bottom of the valley, clearly indicating that this is the most susceptible area (Fig. 9). In contrast, the large sinkholes with degraded edges located in the margins of the valley and largely integrated in the drainage network, are old geomorphic features, probably formed under different conditions (Pallí and Trilla, 1979), which would explain their limited predictive utility. The largest historical sinkhole occurred in 1872, with an axial length of 92 m. A total of six sinkholes have been reported after 1959. This value indicates temporal and spatial-temporal probabilities of 0.1 sinkholes yr^{-1} and 0.01 sinkholes km^{-2} y^{-1}, considering the polygon that embraces all the inventoried depressions (6.7 km^2). These hazard parameters should be considered minimum values since (1) the sinkhole inventory is incomplete; (2) most sinkholes are expected to occur in the valley floor; (3) the time span considered is a maximum value.

Regarding the temporal relationship between subsidence events and the hydrological regime, Sanz (1985) and Brusi et al. (1987, 1990), based on historical data, documented a higher frequency of sinkhole occurrence during dry periods in the Banyoles Lake basin, which is the main discharge zone of the artesian Garrotxa-Banyoles aquifer. Recently, Linares et al. (2017) found a good correlation between temporal sinkhole clusters in the Fluvia Valley and drought periods as revealed by precipitation, river discharge and piezometric data. In the SMCV, Fort (1998), Abellán and Campos (2008), and Abellán (2010), based on historical data previous to the oldest precipitation records, also report a temporal association between droughts and sinkhole events. Unfortunately, the number of collapse events of known age occurred during the precipitation-instrumental period is too small to reinforce this observation (Fig. 12). Two events reported in 1978 and 1980 occurred drought years, the 1994-95 events falls within normal years and two poorly documented collapses roughly situated around 2006 also correlate with a drought period (see Supplementary Data 3).

6.5. Electrical resistivity survey

A 480 m long ERI section was acquired across a large and old sinkhole in order to obtain information on its internal structure. The selected depression is a caprock sinkhole located NW of Falgons, in the western forested slopes of the valley underlain by Banyoles Marls (Fig. 14). It forms part of a prominent NW-SE oriented sinkhole alignment. The ERI line was roughly centred in the centroid of the sinkhole and followed the major axis of the depression. Its trace was conditioned by the distribution of a fire-break and a track, with a curved northern section (Fig. 14B, C).

The most remarkable feature of the ERI section is the presence of widespread inversion artifacts that blurs the stratigraphic signature. It should be noted that the Occam’s inversion imposes smoothed resistivity variations among the adjacent cells of the model. However, in areas with sharp lateral changes in resistivity related to tectonic or collapse faults, this unrealistic assumption results in the occurrence of artificial high- and low-resistivity nodes that overprint the actual resistivity configuration of the subsoil. Nonetheless, the identification of such inversion artifacts allows the identification of fault zones (e.g., Sevil, 2018; Zarroca et al., 2012, 2017).

The inverted resistivity model images a deeply rooted collapse structure 160-180 m across bounded by subvertical normal faults, probably a single ring fault in 3D). The boundaries of the collapse structure can be inferred at the edge of the sharper inversion artifacts (Fig. 14A). The subsidence structure affects the Banyoles Marls, characterized by a low-resistivity of the order of 25-50 Ohm-m. At the margins of the collapse, the bedrock is covered by a thin higher-resistivity material (>100 Ohm-m), corresponding to colluvial deposits (black dotted line in Fig. 14A). The image does not capture the top of the Beuda Gypsum, which should have significantly higher resistivity (>150 Ohm-m) than the overlying Banyoles Marls. Although the bottom of the resistivity image is poorly constrained by data, it suggests that the top of Beuda Gypsum should lies deeper than 120 m at the site.

The inferred collapse faults, which apparently accommodate most of the throw, juxtapose the medium-resistivity Banyoles Marls of the sinkhole margins, against low-resistivity clayey sinkhole-fill deposits with an uncertain thickness that may exceed 30 m (Fig. 14A). The resolution of the ERI is not high enough to elucidate whether the collapsed caprock has behaved as a rigid block or if it has experienced significant internal deformation and brecciation. It is not possible to estimate the total vertical displacement of the structure using the position of the Banyoles Marls on both sides of the collapse faults. However, the thickness of the sinkhole fill provides a minimum estimate of the total subsidence and the thickness of Beuda Gypsum removed by dissolution (30 m). This value, together with the sinkhole area, yields a minimum volume of Beuda Gypsum dissolved by deep-seated instrstratal dissolution of ca. $0.6 \cdot 10^6$ m^3.

7. Discussion

7.1. The aquifer system with hypogene and epigene evaporite karst

The Garrotxa-Banyoles aquifer system has its main recharge area in the elevated Garrotxa limestone massif of the Pyrenees (Fig. 5). The infiltrated groundwater flows southwards along a deep and confined limestone aquifer towards the main discharge area associated with the Banyoles Lake, which is located in a different surface drainage basin (i.e., groundwater traverses a major topographic divide) and geological domain (Ebro Basin). In the Fluvia River valley area, the limestone aquifer (Girona Fm.) is confined by a thick aquiclude, which is overlain by the evaporitic Serrat and Beuda Formations. In this sector, where there is no hydraulic connection between the carbonate and evaporitic formations, the evaporites are affected by a well-developed epigenic karst related to local recharge from the surface (Gutiérrez et al., 2016). To the south the aquiclude overlying the limestone aquifer rapidly pinches out and the 200-300 m thick Beuda Gypsum is in direct contact with the carbonate aquifer. Here, the carbonate and gypsum aquifer system is confined by the Banyoles Marls that reach more than 400 m in thickness. In the discharge areas of the southern sector, the fresh groundwater from the confined carbonate aquifer flows upwards traversing the overlying Beuda Gypsum and causing its hypogene karstification. Thus, the Eocene evaporitic formations associated with the Garrotxa-Banyoles aquifer system show two different karst types (epigene and hypogene) determined by rapid thickness and facies changes related to the asymmetric configuration of the foreland basin (Carrillo et al., 2014). This context offers the opportunity to compare sinkholes related to the hypogene and epigene karstification of the same evaporitic succession in nearby zones. In the hypogene environment, sinkholes are mainly related to the interstratal karstification of the Beuda Gypsum and are spatially associated with the groundwater discharge areas: (1) the Banyoles Lake basin, which is the main and permanent discharge area, controlled by the Camos-Celra Fault (e.g., Canals et al., 1990; Brusi et al., 1987); (2) the SMCV and the Espolla spring, both hydraulically connected (Fig. 6), which function as temporary discharge areas (overflow springs or trop plains) during periods of high piezometric level.

The linkage between the distant recharge and discharge areas of the Garrotxa-Banyoles artesian aquifer system was corroborated in previous investigations using isotopic tracers (^{18}O, ^{3}H; Sanz et al., 1982; Sanz and Trilla, 1982). Moreover, hydrochemical evidence, including new data presented in this work, reveals that in the discharge and sinkhole areas, the Beuda Gypsum is mainly karstified by ascending transverse groundwater flows derived from the underlying carbonate aquifer. These rising and aggressive cross-formational flows experience a significant increase in sulphate concentration in a short distance along the flow path, from around 300 mg/l to as much as 1500 mg/l.

7.2. Origin and characteristics of the sinkholes in the SMCV

The N-S-oriented SMCV has a peculiar sinkhole field associated with one of the discharge areas of the confined aquifer system and an E-W oriented anticline, with the axis located in the central sector of the valley (Fig. 11). In the majority of the valley, the Beuda Gypsum is confined by a caprock of Banyoles Marls that reaches more than 200 m in thickness. In the central sector of the valley floor (axial zone of the anticline), the caprock of Banyoles Marls has been removed by erosion in recent geological times, exposing the Beuda Gypsum. This is the sector where the present-day temporary springs of the regionally confined limestone aquifer area located. A total of 94 sinkholes have been inventoried in the sinkhole field of the SMCV, covering around 6.7 km^2. The most striking feature of the mapped dolines is the presence of numerous hectometre-scale caprock-collapse sinkholes related to the hypogene karstification of the Beuda Gypsum and the foundering of the overlying Banyoles Marls. These are mostly circular to subcircular sinkholes that may be perched in the slopes at high elevation above the valley floor. The large size of these depressions, as much as 300 m across, account for the high areal density of the sinkholes (10.3%), despite the moderate sinkhole density by number (14 sinkholes/km^2). The large sinkholes locally occur in areas where the Beuda Gypsum is overlain by a caprock of marls more than 200 m thick, indicating that they: (1) are related to deep-seated hypogene and interstratal karstification of evaporites; and (2) are underlain by large collapse structures that may reach more than $9 \cdot 10^6$ m^3 in volume. The ERI survey carried out across a large sinkhole developed in outcrops of Banyoles Marls images a large collapse structure 160 m across bounded by subvertical failure planes (ring fault? margins of a breccia pipe?) with an estimated vertical displacement of 30-50 m (Fig. 14). These latter figures support the concept that the sinkholes are related to the interstratal dissolution of large volumes of gypsum (ca. $1 \cdot 10^6$ m3), probably large hypogene chambers (e.g., Kempe, 1996). It is likely that collapse processes also strata of the Beuda Gypsum, since solutional cavities in this hypogene context are expected to grow from the base of the karst unit.

The karst depressions show clear spatial variations across the sinkhole field (Fig. 11). In the central sector of the valley floor, where the level of erosion has reached the Beuda Gypsum (axial zone of the anticline), the sinkholes show higher density by number and smaller dimensions. This feature can be attributed to several factors: (1) lack of mechanically resistant caprock and the development of cover-collapse sinkholes in a mantled karst setting; (2) epigene karstification by downward flows overprinting the hypogene cavities developed before the erosional removal of the confining caprock; (3) higher impact of the changes in the piezometric level associated with periods of rising groundwater flow and downward infiltration. In the valley margins and the northern and southern sectors of the valley, where the Beuda Gypsum is overlain by a thick caprock of Banyoles Marls, sinkholes show a lower density by number, but much larger dimensions and higher areal density. This pattern may be explained by the lack of cover-collapse sinkholes and the caprock thickness increase. In sectors with thick caprock, only large cavities may reach the surface by upward stoping since collapse processes entail a volume increase (bulking effect) and the resulting breccias tend to choke the voids. This factor is expected to be more pronounced in hypogene settings with recharge from below, where cavities tend to initiate at the base of the karst formation. Geomorphic mapping also reveals that sinkholes tend to occur associated with channels (Fig. 9). Around 46% of the sinkholes are located at a distance of less than 50 m from the nearest channel (see Supplementary Data SD2). This may be related to several mechanical and hydrologic factors: (1) thinner package of sediments above the karstified Beuda Gypsum; (2) upward groundwater discharge tends to focus in topographically lower areas, leading to more intense karstification and the mechanical weakening of the overlying strata (Klimchouk, 2007); (3) higher surface water infiltration during periods of low piezometric level, favouring dissolution and subsidence processes.

Frequency-size relationships of subsidence sinkholes have been analysed in a limited number of regions, despite their relevance from the hazard perspective. To our knowledge, all the published regressions, as well as the one developed for the sinkhole inventory of the SMCV, show that the relationships between the sinkhole major axis versus relative cumulative frequency can be modelled with a high goodness of fit ($R^2>0.9$) by log-normal functions (Fig. 13). A similar result can be expected for other morphometric parameters such as sinkhole area. This type of exponential relationships, illustrating the "rarity" of large-magnitude events and the "commonness" of low-magnitude events, are found for other hazardous processes, including earthquakes (Gutenberg and Richter, 1954), volcanic eruptions (Pyle, 2000), landslides (Korup, 2012) or floods (Costa and Baker, 1981). Figure 13 allows to compare the sinkholes of the hypogene gypsum karst of the SMCV with the sinkholes inventoried in other epigene limestone and evaporite karst regions. The distribution of the regression lines shows the impact of the nature, thickness and mechanical strength of cavity-roof sediments on the size of the sinkholes. The smaller depressions are the cover-collapse sinkholes of the mantled karst of the Val d'Orléans, central France, developed in a weak and thin (6-10 m) sandy alluvial cover mantling karstified limestone (Gombert et al., 2015). The cover-collapse sinkholes of the Hamedan plains, Zagros Mountains, Iran, mainly induced by aquifer over-exploitation and the consequent water table decline, reach significantly larger dimensions. In this alluvial karst setting the cavernous limestone is overlain by thick and cohesive alluvium that reaches more than 100 m in thickness (Heidari et al., 2011; Taheri et al., 2015). In the Ambal salt pillow, Zagros Mountains, Iran, collapse sinkholes are related to upward stoping of cavities developed in salt beneath a residual caprock, mainly consisting of distorted gypsum and clayey sediments (Gutiérrez and Lizaga, 2016). The regression line of the sinkholes mapped in the epigene evaporite karst of the Fluvia Valley, north of the study area, shows a markedly different slope and intersects to or converges with the lines of the areas with smaller sinkholes. This can be attributed to the broad range of stratigraphic contexts and sinkhole types of the area, inasmuch subsidence affects to weak and thin alluvial cover, thickened and cemented alluvium, and thick caprocks of marls, sandstones or even Pleistocene basalts (Gutiérrez et al., 2016; Fabregat et al., 2017). The regression line of the SMCV is displaced to the right, reflecting the much larger size of the sinkholes. Here, sinkholes are mainly related to deep-seated hypogene karstification of gypsum and the collapse of a thick stratigraphic succession, including a caprock of marls, locally more than 200 m thick, and probably also part of the gypsum unit.

7.3.Sinkholes in hypogene and epigene karst settings

Epigene and hypogene dissolution occurs in different sectors of the groundwater flow system with contrasting types and patterns of groundwater flow, producing caves with distinctive features that may have some impact on the characteristics and patterns of the associated sinkholes:

- Sinkholes related to hypogene dissolution tend to occur in areas disconnected from the recharge areas of the aquifer systems (e.g., Vigna et al., 2010), and are frequently associated with the discharge zones of artesian aquifers. In the case of carbonate aquifers, the groundwater in discharge areas is commonly saturated with respect to calcite and unable to dissolve limestone. In these contexts, dissolution and sinkhole development is generally related to renewed aggressiveness by the incorporation of deeply-sourced fluids (e.g., Salvati and Sasowsky, 2002; Gary and Sharp, 2006;

Frumkin et al., 2015). This limitation rarely affects hypogene evaporitic systems, since dissolution is commonly caused by upward aggressive flows derived from an underling non-evaporitic aquifer. In the case of the Garrotxa-Banyoles aquifer system, there is clear spatial association between the sinkhole fields produced by evaporite hypogene karstification and the groundwater discharge areas (Fig. 5): the SMCV, Espolla spring and the Banyoles Lake Basin. The association of sinkhole fields related to hypogene evaporite dissolution and groundwater discharge areas of artesian aquifers has been documented in other regions worldwide. These groundwater discharge areas are frequently controlled by topographic lows created by fluvial incision and/or subsidence depressions formed by the downdip migration of dissolution fronts in homoclinal structures. In NE England, sinkhole development affects a 140 km long and 3 km wide groundwater discharge area associated with river valleys, where upward aggressive flow from a limestone formation traverses the overlying Permian gypsum formations (Cooper, 1986, 1998). Here, Cooper et al. (2013) find a spatial correlation between sulphate-rich springs and sinkhole clusters, including recent collapse events. In the eastern margin of the Pecos River valley, Delaware Basin, New Mexico, the large sinkhole lakes of the Bottomless State Park are fed by underwater springs of the Roswell artesian basin (Fig. 15A). Groundwater rises from the confined San Andrés Limestone and traverses the overlying gypsum and salt layers of the Permain Seven Rivers Formation. These sinkholes are associated with a monoclinal escarpment generated by the gravitational flexure of strata atop a downdip-propagating dissolution front (Land, 2003). Layla Lakes in the Interior Homocline of Saudi Arabia are large sinkholes restricted to a spring area and related to hypogene dissolution of anhydrite in the Arab and Hith formations by upward transverse flows derived from the underlying limestone aquifer. These lakes that used to be fed by sulphate–rich springs have been drained by groundwater overexploitation, exposing dramatic gypsum precipitates on their walls (Kempe and Dirks, 2008; Schleusener et al., 2013).

- Hypogene dissolution tends to produce spatially restricted caves but with a much higher density of solutional voids than epigene caves. Klimchouk (2006) compared morphometric parameters of representative hypogene and epigene caves. He found that passage network density (cave length versus area of the cave field) and cave porosity (volume of cavities versus volume of the cave block) are one order of magnitude higher in hypogene caves. Similarly, average areal coverage (area occupied by passages in plan-view versus area of cave field) is about five times higher in confined/epigene settings. Klimchouk (2003) and Frumkin and Fischhendler (2005) contend that hypogene karst tends to form in dense clusters separated by regions of minimal karst development. In contrast, epigene karst is generally expressed through more widely distributed features, where descending meteoric waters attempt to exploit all the available discontinuities and converge at depth. Consequently, collapse sinkholes related to hypogene karstification are expected to show different spatial patterns, including a tendency to form clusters or sinkhole fields with a high density of depressions. This feature can be analysed quantitatively through the nearest neighbour index (NNI), but it should be taken into account that this parameter is scale dependent. For instance, the calculation of the NNI in a large region including dense sinkhole fields separated by extensive tracts of land devoid of karst depressions would indicate high clustering, whereas a specific sinkhole field may yield a completely different NNI, indicating low clustering. In the region of the Garrotxa-Banyoles karst system, sinkholes form clusters associated with the discharge areas, but in the specific sinkhole field of the SMCV the karst depressions show a random distribution (NNI of 1.3), quite similar to the epigene evaporite karst of the Fluvia River valley (NNI of 1.1) (Gutiérrez et al., 2016), with a much larger area (122 km^2 vs. 6.7 km^2). Sinkhole clusters have been documented in several hypogene evaporite karst regions. In the extensive outcrops of the Castile Formation of the Gypsum Plain (ca. 1800 km^2), Delaware Basin, karst features are strongly clustered (NNI of 0.4). Approximately 40% of the region exhibits no karst development (<1 feature/km^2), whereas two small regions exhibit a very high density of karst features (>40 features/km^2) (Stafford et al., 2008a). Speleogenesis in the Castile Formation is dominated by transverse hypogene flows derived from the underlying detrital Bell Canyon Fm. (Stafford et al., 2008b). In the hypogene gypsum karst of NE England, sinkholes form dense clusters separated by extensive areas with no evidence of dissolution-induced subsidence. These scattered sinkhole fields in which the depressions show an overall grid pattern (Cooper, 1986) seem to reflect the distribution of non-accessible maze caves. In the hypogene gypsum karst of Ukraine, sinkholes form clusters in localised areas underlain by spatially restricted maze caves. Breakdown structures mapped in several caves indicates that sinkholes tend to occur above outlet cupolas that have breached the bottom of the supra-gypsum formation, rather than by the stoping of the widest passages. These solution cupolas or dome pits tend to have a rather regular distribution controlled by the fracture system (Klimchouk and Andrejchouk, 2005). Sinkhole clustering is also found in other hypogene systems, such as the evaporite karst of the Interior Homocline of Saudi Arabia (Kempe and Dirks, 2008), the Zacatón system in Mexico (Gary and Sharp, 2006) (Fig. 15B) or the Obruks of Central Anatolia (Serdar et al., 2009; Dogan and Yilmaz, 2011) (Fig. 15C).

- Hypogene settings are particularly favourable for the development of large collapse sinkholes and deep collapse structures or breccia pipes, due to the frequent concurrence of the following factors: (1) dissolution typically occurs in deep-seated confined environments by upward flow; (2) hypogene karstification frequently generates large isolated chambers; (3) the soluble formation affected by dissolution may be overlain by a thick resistant caprock of non-soluble strata; (4) the development of solution cavities typically start at the base of the karst formation, so collapse structures may propagate through a thick stratigraphic succession including karst bedrock and caprock. When dissolution occurs at high depth and below resistant rocks, only cavities with large span and volume are able to reach the surface by upward stoping before they become choked by the bulking effect associated with brecciation. In the SMCV, caprock collapse sinkholes reach more than 300 m across and are underlain by large collapse structures that may reach more than $10 \cdot 10^6$ m^3, involving a thick caprock and probably also the upper part of the Beuda Gypsum (**Fig. 13**). Large collapse sinkholes frequently occur associated with dissolution fronts in homoclinal structures. In the Interior Homocline of Saudi Arabia, dissolution of the E-dipping Hith Formation by upward flow coming from the underlying carbonate formations cause a progressive down-dip migration of a dissolution front. The gravitational flexure of the overlying formations atop the dissolution front results in the development of a west-facing monoclinal fold and escarpment as much as 550 km long with prominent geomorphic expression. The caprock in the monoclinal escarpment is affected by numerous ground ruptures related to extension on the outer arch of the drape fold (fissures, scarps, crestal grabens) and is locally punctured by clusters of hectometre-scale caprock collapse sinkholes (e.g., Dahl Hit, Al Khafs; Memesh et al., 2008; Kempe and Dirks, 2008; Warren, 2016) (Fig. 15D). A similar situation is found in the monoclinal drape fold that controls the Seven Rivers Escarpment, at the east margin of the Pecos River valley. Hypogene evaporite dissolution in the Permian Seven Rivers Formation by rising groundwater coming from an underlying limestone of the San Andres artesian aquifer has created large cavities and the hectometre-scale collapse sinkholes that host the Bottomless Lakes (Land, 2003) (Fig. 15A). However, sinkholes in hypogene settings may also have regular dimensions, like those developed above the gypsum maze caves of western Ukraine, consisting of labyrinthic networks of passages with limited width controlled by joints (Klimchouk and Andrejchouk, 2005). Moreover, very large collapse sinkholes also occur in association with epigene caves, including some of the largest sinkholes on Earth like the tiankengs of China (Xuewen and Waltham, 2005).

The discussion presented above suggests that sinkholes in hypogene settings tend to display different features to those formed in epigene karst systems, but these cannot be considered as diagnostic criteria. In most cases, unravelling the type of karst responsible for the development of sinkholes in a specific area requires proper understanding of the regional geology, its hydrostratigraphy and the groundwater flow system, for which hydrochemical data may provide relevant clues. Further investigations about this poorly explored issue may provide useful tools for sinkhole hazard analysis and spelogenetic interpretations.

8. Conclusions

In the Garrotxa-Banyoles artesian aquifer system there are sectors with epigene and hypogene evaporite karst, whose distribution is controlled by the rapid wedging out of a low-permeability unit situated between the confined limestone aquifer and the overlying evaporitic formations. In the hypogene sector, sinkholes are spatially associated with permanent and temporary groundwater discharge zones, including the SMCV analysed in this work. Sinkholes in the epigene and hypogene environments show different characteristics (e.g., dimensions) and spatial patterns (widespread versus spatially restricted, respectively).

The regional geology, hydrostratigraphy, hydrochemical data and geomorphological evidence indicate that deep-seated hypogene gypsum karstification in the SMCV is related to aggressive flows that ascend from the regional limestone aquifer and traverse the overlying gypsum formation, extensively capped by a thick caprock of marls.

Hypogene karstification of the gypsum leads to the development of large deep-seated cavities and caprock-collapse sinkholes as much as 300 m across, locally affecting a succession of marls more than 200 m thick. These sinkholes, as supports an ERI survey, are underlain by deep collapse structures ($>9\cdot10^6$ m^3), probably rooted at the base of the evaporitic unit. Although these sinkholes form regional clusters associated with the groundwater discharge zones, they show a non-clustered distribution within the sinkhole field.

The results of this work and a literature review, suggests that sinkholes tend to display different characteristics in hypogene and epigene settings. In the former environments, sinkholes tend to form dense clusters associated with groundwater discharge (or paleodischarge) areas, separated by regions of minimal karst development. However, the karst depressions within these spatially restricted sinkhole fields are not necessarily clustered (i.e. clustering is scale dependent). Moreover, deep-seated hypogene karst tends to produce very large caprock- and bedrock-collapse sinkholes, with frequency-size relationships that can be satisfactorily modelled by log-normal regressions.

Acknowledgements

This work has been supported by project CGL2017-85045-P (Ministerio de Economía, Industria y Competividad, Gobierno de España). The authors are very thankful to the Institut Cartogràfic i Geològic de Catalunya (ICGC), Agència Catalana de l'Aigua (ACA) and the City Hall of Sant Miquel de Campmajor for providing copies of unpublished geotechnical reports. We would like to thank Dr. Luis Auqué for helping in the hydrochemical studies and Mr. Joan Fort i Olivella for providing support and valuable data. I.F. has a FPI grant (BES-2014-068836) of the Spanish Government. M.Z. has a Serra Húnter fellowship at the Universitat Autònoma de Barcelona (UAB). Á.G.A. has a PhD grant (C237/2016) from the Government of Aragón.

References

Abellán, J.A., 2010. Històries, llegendes i curiositats del estanyols i brolladors del Pla de l'Estany. Revista de Banyoles 918, 26–33.

Abellán, J.A., Campos, M., 2008. Zona Lacustre de l'Estany de Banyoles. Estanys, estanyols i llacunes. Consell Comarcal del Pla de l'Estany, Banyoles, 21 p.

Acero, P., Gutiérrez, F., Galve, J. P., Auqué, L. F., Carbonel, D., Gimeno, M. J., Gómez, J.B., Asta, M.P., Yechieli, Y., 2013. Hydrogeochemical characterization of an evaporite karst area affected by sinkholes (Ebro Valley, NE Spain). Geologica Acta: an international earth science journal 11(4), 389–407.

Audra, P., Mocochain, L., Bigot, J.V., Nobécourt, J.C., 2009. Hypogene cave patterns. In: Klimchouk, A., Ford, D. (Eds.), Hypogene speleogenesis and karst hydrogeology of artesian basins. Ukranian Institute of Speleology and Karstology Special Paper 1, pp. 17–22.

Bach, J., Brusi, D., Sanz, M., Trilla, J. 1986. Ejemplo de sistema kárstico tipo "trop plein" (La Garrotxa-Banyoles). Jornadas sobre el Karst en Euskadi. Tomo I, 137–151.

Ball J.W., Nordstrom, D.K., 2001. User's manual for WATEQ4F, with revised thermodynamic data base and test cases for calculating speciation of major, trace, and redox elements in natural waters. USA, US Geological Survey Open File Report, 91–183.

Barnolas, A., Teixell, A., Durán, H., Escuer Solé, J., 1994. Mapa y Memoria del Mapa Geológico de España. Escala 1:50.000. Nº 295 (38-12) Bañolas. Instituto Geológico y Minero de España. Madrid.

Barnolas, A., Pujalte, V., 2004. La Cordillera Pirenaica. En: Vera, J.A., (Ed.) Geología de España. Sociedad Geológica de España –Instituto Geológico y Minero de España, Madrid, 233–343.

Basso, A., Bruno, E., Parise, M., Pepe, M., 2013. Morphometric analysis of sinkholes in a karst coastal area of southern Apulia (Italy). Environ. Earth Sci. 70 (6), 2545–2559.

Bischoff, J.L., Julià, R., Shanks, W.C., Rosenbauer, R.J., 1994. Karstification without carbonic acid: Bedrock dissolution by gypsum-driven dedolomitization. Geology 22, 995–998.

Brinkmann, R., Parise, M., Dye, D., 2008. Sinkhole distribution in a rapidly developing urban environment: Hillsborough County, Tampa Bay area, Florida. Eng. Geol. 99, 169–184.

Brusi, D., Bach, J., Sanz, M., 1990. Itinerari Geològic de Banyoles. Descoberta del funcionament del Sistema lacustre. Eumo Editorial, Barcelona,124 p.

Brusi, D., Maroto, J., Vila, X., 1992. L'estany de Banyoles. In: Pallí, L., Brusi, D. (Eds), El medi natural a les terres gironines. Universitat de Girona, pp. 117–133.

Brusi, D., Pallí, L., Sanz, M., 1987. Caracterización de inestabilidades gravitatorias en el área de Banyoles. III Reunión Nacional de Geología Ambiental y Ordenación del Territorio, Valencia, vol. 2, pp. 1021–1034.

Canals, M., Got, H., Julià, R., Serra, J., 1990. Solution-collapse depressions and suspensates in the limnocrenic lake of Banyoles (NE Spain). Earth Surface Processes and Landforms 15, 243-254.

Carrillo, E. 2009. Unidades evaporíticas de la Zona Surpirenaica Oriental (Área de La Garrotxa). Geogaceta 47, 73–76.

Carrillo, E., Rosell, L., Ortí, F., 2014. Multiepisodic evaporite sedimentation as an indicator of paleogeographical evolution in foreland basins (South-eastern Pyrenean basin, Early-Middle Eocene). Sedimentology 61, 2086–2112.

Cirés, J., Gimeno, D., Díaz, N., Mallarach, J.M., Solà, J., Montaner, J., Viñals, E., Mató, E., 2002. Santa Pau 295-1-1 (75-23). Mapa Geològic de Catalunya. 1:25.000. Institut Cartogràfic de Catalunya.

Cooper, A.H., 1986. Subsidence and foundering of strata caused by the dissolution of Permain gypsum in the Ripon and Beadale areas, North Yorkshire. In: Harwood, G.M., Smith, D.B. (Eds.), The English Zechstein and Related Topicws. Geological Society Special Publication 22, pp. 127–139.

Clark, P.J., Evans, F.C., 1954. Distance to Nearest Neighbor as a Measure of Spatial Relationships in Populations. Ecology 35(4), 445–453.

Cooper, A.H., 1998. Subsidence hazards caused by the dissolution of Permian gypsum in England: geology, investigation and remediation. In: Maund, J.G., Eddleston, M. (Eds.), Geohazards in Engineering Geology. Geological Society, London. Engineering Geology Special Publication 15, 265–275.

Cooper, A.H., Odling, N.E., Murphy, P.J., Miller, C., Greenwood, C.J., Brown, D.S., 2013. The role of sulfate-rich springs and groundwater in the formation of sinkholes over gypsum in eastern England. In: Land, L., Doctor, D.H., Stephenson, J.B. (Eds.), Sinkholes and the Engineering and Environmental Impacts of Karst. National Cave and Karst Research Institute, Carlsbad, New Mexico, pp. 141–150.

Constable, S., Parker, R. L., Constable, C. G. 1987. Occam's inversion: A practical algorithm for generating smooth models from electromagnetic sounding data. Geophysics 52, 289–300.

Costa, J., Baker, V., 1981. Surficial Geology. John Wiley & Sons, New York, 497 p.

Cvijic, J., 1893. Das Karstphänomen. Versuch einer morphologischen Monographie. Geographische Abhandlungen. E. Hölzel, Stuttgart, 114 pp.

Dahlin, T., Zhou, B. 2004. A numerical comparison of 2D resistivity imaging with 10 electrode arrays. Geophysical Prospecting 52, 379–398.

Denizman, C.A.N., 2003. Morphometric and spatial distribution parameters of karstic depressions, Lower Suwannee River Basin, Florida. Journal of cave and karst studies 65(1), 29–35.

Dogan, U., Yilmaz, M., 2011. Natural and induced sinkholes of the Obruk Plateau and Karapinar-Hotamis Plain, Turkey. Journal of Asian Earth Sciences 40, 496-508.

Dublyansky, Y.V., 2014. Hypogene speleogenesis. Discussion of definitions. Karst Waters Institute Special Publication 18, 1–3.

ESRI., 2017. ArcGIS. Redlands (CA): Environmental System Research Institute. Available from: http:// www.esri.com/software/arcgis/arcinfo/index.html

Fabregat, I., Gutiérrez, F., Roqué, C., Comas, X., Zarroca, M., Carbonel, D., Guerrero, J., Linares, R., 2017. Reconstructing the internal structure and long-term evolution of hazardous sinkholes combining trenching, electrical resistivity imaging (ERI) and ground penetrating radar (GPR). Geomorphology 285, 287–304.

Ford, D.C., 2006. Karst geomorphology, caves and cave deposits: A review of North American contributions during the past half century. In: Harmon, R.S., Wicks, C.W. (Eds.), Perspectives on Karst Geomorphology, Hydrology and Geochemistry, GSA Special Paper 404pp. 1–14. Boulder. Colorado.

Fort, J., 1998. La Vall de Campmajor. Quaderns de la Revista de Girona, núm. 80. Sèrie: Monografíes, núm. 47. Diputació de Girona/Caixa de Girona. (Eds.), 96 p. ISBN: 84-86812-90-9.

Frumkin, A., Fischhendler, I., 2005. Morphometry and distribution of isolated caves as a guide for phreatic and confined paleohydrological conditions. Geomorphology 67, 457–451.

Frumkin, A., Zaidner, Y., Na'aman, I., Tsatskin, A., Porat, N., Vulfson, L., 2015. Sagging and collapse sinkholes over hypogenic hydrothermal karst in a carbonate terrain. Geomorphology 229, 45-57.

Gary, M.O., Sharp, J.M., 2006. Volcanogenic karstification of Sistema Zacatón, Mexico. In: Harmon, R.S., Wicks, C. (Eds.), Perspectives on karst geomorphology, hydrology and geochemistry. Geological Society of America Special Paper 404, pp. 79–89.

Gombert, P., Orsat, J., Mathon, D., Alboresha, R., Al Heib, M., Deck, O., 2015. Role des efondrements karstiques sur les desordres survenus sur les digues de Loire dans le Val D'Orleans (France). Bulletin of Engineering Geology and Environment 74, 125-140.

Griffiths, D. H., Barker, R. D. 1993. Two-dimensional resistivity imaging and modeling in areas of complex geology. Journal of Applied Geophysics 29, 211–226.

Gutenberg, B., Richter, C.F., 1954. Frequency and energy of earthquakes. In: Gutenberg, B., Richter, C.F. (Eds.), Seismicity of the Earth and Associated Phenomena, 2nd ed. Princeton, N.J., Princeton University Press, pp. 17–19.

Gutiérrez, F., 2016. Sinkhole hazards. In: Cutter, S.L. (Ed.), Oxford Research Encyclopedia of Natural Hazard Science. Oxford University Press, Oxford, 1–92 pp.

Gutiérrez, F., Fabregat, I., Roqué, C., Carbonel, D., Guerrero, J., García-Hermoso, F., Zarroca, M., Linares, M., 2016. Sinkholes and caves related to evaporite dissolution in a stratigraphically and structurally complex setting, Fluvia Valley, eastern Spanish Pyrenees. Geological, geomorphological and environmental implications. Geomorphology 267, 76–97.

Gutiérrez, F., Guerrero, J., Lucha, P., 2008. A genetic classification of sinkholes illustrated from evaporite paleokarst exposures in Spain. Environmental Geology 53, 993–1006.

Gutiérrez, F., Lizaga, I., 2016. Sinkholes, collapse structures and large landslides in an active salt dome submerged by a reservoir: The unique case of the Ambal ridge in the Karun River, Zagros Mountains, Iran. Geomorphology 254, 88–103.

Heidari, M., Khanlari, G.R., Taleb, A.R., Momeni, A.A., 2011. The formation of cover collapse sinkholes in North of Hamedan, Iran. Geomorphology 132, 76–86.

Hyatt, J.A., Wilkes, H.P., Jacobs, P.M., 1999. Spatial relationships between new and old sinkholes in covered karst, Albany, Georgia, USA. In: Beck, B.F., Herring, J.G. (Eds.), Hydrogeology and Engineering Geology of Sinkholes and Karst. Balkema, Rotterdam, pp. 37–44.

Höbig, N.,Weber, M.E., Kehl, M.,Weniger, G.-C., Julià, R.,Melles, M., Fülöp, R.-H.,Vogel, H., Reicherter, K., 2012. Lake Banyoles (northeastern Spain): a Last

Glacial to Holocene multi-proxy study with regard to environmental variability and human occupation. Quaternary International 274, 205–218.

IGME, 1986. Estudio hidrogeológico de las cuencas altas de los ríos Ter, Fluvià y Muga. Provincia de Gerona. Instituto Tecnológico GeoMinero de España.

IGME, 1990. Estudio hidrogeológico de los acuíferos del lago de Banyoles (Gerona). Años 1988, 1989, 1990. Proyecto de Actualización Infraestructura hidrogeológica, vigilancia y catálogo de acuíferos. Tomo I, Memoria. Instituto Tecnológico GeoMinero de España, 374 p.

Julià, R., 1980. La conca lacustre de Banyoles–Besalú. Monografies del Centre d'Estudis Comarcals de Banyoles, 187 p.

Kemmerly. P,R., 1982. Spatial analysis of a karst depression population; clues to genesis. Geol. Soc. Ameri. Bull. 93, 1078–1086.

Kempe, S., 1996. Gypsum karst of germany. International Journal of Speleology 25, 209–224.

Kempe, S., Dirks, H., 2008. Layla Lakes, Saudi Arabia: the world-wide largest lacustrine gypsum tufas. Acta Carsologica 37, 7–14.

Klimchouk, A.B., 2003. Conceptualization of speleogenesis in multi-story artesian systems: a model of transverse speleogenesis. Speleogenesis and Evolution of Karst Aquifers 1, 1–18.

Klimchouk, A.B., 2006. Unconfined versus confined speleogenetic settings: variations of solution porosity. International Journal of Speleology 35, 19–24.

Klimchouk, A.B., 2007. Hypogene speleogenesis: hydrogeological and morphogenetic perspective. National Cave and Karst Research Institute. Special paper 1, 106 p.

Klimchouk, A., Andrejchouk, V., 2005. Karst breakdown mechanisms from observations in the gypsum caves of the Western Ukraine: implications for subsidence hazard assessment. Environmental Geology 48, 336–359.

Klimchouk, A., Palmer, A.N., De Waele, J., Auler, A.S., Audra, P. (Eds.) 2017. Hypogene karst regions and caves of the World. Springer, 911.

Korup, O., 2012. Landslides in the Earth system. In: Clague, J.J., Stead, D. (Eds.), Landslides. Types, mechanisms and modelling. Cambridge University Press, Cambridge, pp. 10–22.

Kranjc, A., 2013. Classification of closed depressions in carbonate karst. In: Frumkin, A. (Eds.), Kart Geomorphology. Treatise on Geomorphology, vol. VI, 104–111.

LaBrecque, D., Miletto, M., Daily, W., Ramirez, A., Owen, E. 1996. The effects of noise on Occam's inversion of resistivity tomography data. Geophysics 61, 538–548.

Land, L.A., 2003. Evaporite karst and regional groundwater circulation in the Lower Pecos Valley of Southeastern New Mexico. In: Johnson, K.S., Neal, J.T. (Eds.), Evaporite karst and engineering/environmental problems in the United States. Oklahoma Geological Survey Circular 109, pp. 227–232.

Linares, R., Roqué, C., Gutiérrez, F., Zarroca, M., Carbonel, D., Bach, J., Fabregat, I., 2017. The impact of droughts and climate change on sinkhole occurrence. A case study from the evaporite karst of the Fluvia Valley, NE Spain. Science of the Total Environment 579, 345–358.

Loke, M.H., 2011. Electrical resistivity surveys and data interpretation. In: Gupta, H. (Ed.), Encyclopedia of Solid Earth Geophysics, 2nd Edition. Electrical and Elctromagnetic, Springer-Verlag, pp. 276–283.

Loke, M. H., Chambers, J. E., Rucker, D. F., Kuras, O., Wilkinson, P. B. 2013. Recent developments in the direct-current geoelectrical imaging method. Journal of Applied Geophysics 95, 135–156.

Magdalene, S., Alexander Jr., E.C., 1995. Sinkhole distribution in Winona County, Minnesota revisited. In: Beck, B.F., Person, F.M. (Eds.), Karst Geohazards. Balkema, Rotterdam, pp. 43–51.

Martínez, A., Rivero, L., Casas, A., 1997. Integrated gravity and seismic interpretation of duplex structures and imbricate thrust Systems in the southeastern Pyrenees (NE Spain). Tectonophysics 282, 303–329.

Martínez, A., Samsó, J.M., Zamorano, M., Picart, J., Solà, J., Montaner, J., Mató, E., 2000. Besalú (76–22). Mapa Geològic de Catalunya 1:25.000. Institut Cartogràfic de Catalunya. Barcelona.

Martínez, A., Vergés, J., Clavell, E., Kennedy, J., 1989. Stratigraphic framework of the thrust geometry and structural inversion in the southeastern Pyrenees: La Garrotxa area. Geodinàmica Acta 3(3), 185–194.

Mató. E., Saula, E., Picart, J., Solà, J., Montaner, J., Viñals, E., Samsó, J.M., Serra, J., Llenas, M., Agustí, J., Mallarach, J., 1996. Banyoles (76-23). Mapa Geològic de Catalunya 1:25.000. Institut Cartogràfic de Catalunya. Barcelona.

McConnell H., Horn J.M., 1972. Probabilities of surface Karst. In: Chorley R.J. (Ed.), Spatial Analysis in Geomorphology. Harper and Row, New York, pp. 111–133.

Memesh, A., Dini, S., Gutiérrez, F., Wallace, C.A., 2008. Evidence of large-scale subsidence caused by interstratal karstification of evapotices in the Interior Homocline of Central Saudi Arabia. European Geosciences Union General Assembly. Geophysical Research Abstracts 10, A-02276.

Morellón, M., Anselmetti, F.S., Valero-Garcés, B., Giralt, S., Ariztegui, D., Sáez, A., Mata, M.P., Barreiro-Lostres, F., Rico, M. y Moreno, A., 2014. The influence of subaquatic springs in lacustrine sedimentation: Origin and paleoenvironmental significance of homogenites in karstic Lake Banyoles (NE Spain). Sedimentary Geology, 311, 96–111.

Pallí, L., 1972. Estratigrafía del Paleógeno del Empordà y zonas limítrofes. Publicaciones De Geología. Universitat Autònoma de Barcelona, 338 p.

Pallí, LL., Trilla, J., 1979. Morfogénesis del valle de St. Miquel de Campmajor. Acta Geológica Hispánica 14, 451–456.

Palmer, A.N., 2007. Cave Geology. Cave Books, Dayton, 454 p.

Parkhurst, D.L., Appelo, C.A.J., 2013. Description of input and examples for PHREEQC version 3-A computer program for speciation, batch-reaction, one-dimensional transport, and inverse geochemical calculations. U.S. Geological Survey Techniques and Methods, book 6, chapter A43, 497pp. Available only at http://pubs.usgs.gov/tm/06/a43/

Puig, C., Badia, R., Bernat, E., Diaz, E., Martínez, A., Samsó, J.M., Planagumà, L., Mallarach, J.M., Solà, J., Montaner, J., 2003. Olot (75-22). Mapa Geològic de Catalunya 1:25.000. Institut Cartogràfic de Catalunya.

Puig, C., Mató, E., Saula, E., Picart, J., Montaner, J., Mallarach, J.M., Samsó, J.M., Serra-Kiel, J., 1997a. Amer 295-1-2 (75-24). Mapa Geològic de Catalunya. 1:25.000. Institut Cartogràfic de Catalunya. Barcelona.

Puig, C., Mató, E., Saula, E., Picart, J., Solà, J., Montaner, J., Samsó, J.M., Serra-Kiel, J., Llenas, M., Agustí, J., Mallarach, J.M., 1997b. Canet d'Adri 295-2-2 (76-24). Mapa Geològic de Catalunya. 1:25.000. Institut Cartogràfic de Catalunya. Barcelona.

Puigdefàbregas, C., Muñoz, J. A., Marzo, M., 1986. Thrust belt development in the Eastern Pyrenees and related depositional sequences in the southern foreland basin. In: Allen, P.A., Homewood, P. (Eds.), Foreland basins. Special Publication International Association of Sedimentologists 8, 229–246.

Pyle, D.M., 2000. Sizes of volcanic eruptions. In: Sigurdsson, H., Houghton, B., Rymer, H., Stix, J., McNutt, S. (Eds.), Encyclopedia of Volcanoes. Academic Press, San Diego, CA, pp. 263–269.

Ramos, E., Busquets, P., Verges, J., 2002. Interplay between longitudinal fluvial and transverse alluvial fan systems and growing thrusts in a piggyback basin (SE Pyrenees). Sedimentary Geology 146(1-2), 105–131.

Rehrl, C., Birk, S., Klimchouk, A.B., 2008. Conduit evolution in deep-seated settings: Conceptual and numerical models based on field observations. Water Resources Research 44, W11425.

Roqué, C., Linares, R., Zarroca, M., Pallí, L., 2014. The Olot Volcanic field. In. Gutiérrez, F., Gutiérrez, M. (Eds.), Landscapes and landforms of Spain. Springer, Dordrecht, pp. 249–256.

Salvati, R., Sasowsky, I.D., 2002. Development of collapse sinkholes in areas of groundwater discharge. Journal of Hydrology 264, 1–11.

Sanz, M., 1981. E1 sistema hidrogeológico de Banyoles – La Garrotxa. Unpublished PhD Thesis, Facultad de Ciencias, Universidad Autónoma de Barcelona, Spain, 306 p.

Sanz, M. 1985. Estudi hidrogeològic de la conca de Banyoles – La Garrotxa. Quaderns del Centre d’Estudis Comarcals de Banyoles 1980–1984. Banyoles, vol. 2, 171–250.

Sanz, M. ; Bach, J. Trilla, J., 1982. Aplicación del oxígeno 18 al sistema kárstico de Banyoles-La Garrotxa. Comunicaciones de la Reunión Monográfica sobre el karst de Larra, 243–255. Navarra.

Sanz, M., Trilla, J., 1980. Particularidades hidrogeológicas y limitaciones del uso territorial en un área de la provincia de Girona. Comunicaciones de la 1ª Reunión Nacional de Geología Ambiental y Ordenación del Territorio. Santander.

Sanz, M., Trilla, J., 1982. Consideraciones sobre la dinámica del sistema cárstico de la Garrotxa. III Simposio de Hidrogeología, 475–483. Madrid.

Saula, E., Picart, J., Mato, E., Llenas, M., Lozanitos, M., Berastegui, X., Agustí, J., 1994. Evolución geodinámica de la fosa del Empordà y las Sierras transversales. Acta Geol. Hisp. 29, 55–75.

Schleusener, F., Kempe, S., Dirks, H., Rausch, R., Göbel, P., 2013. Die erdfälle von Layla und Al-Kharj-Einblicke in fie karst-hydrologie des oberen Jura von Saudi-Arabien. Zeitschrift der Fachsektion Hydrologie 18, 271–276.

Serdar, C., Pekkan, E., Ozyurt, N., 2009. Obruks, as giant collapse dolines caised by hypogenic karstification in central Anatolia, Turkey: analysis of likely formation processes. Hydrogeology Journal 17, 327-345

Serra, T.,Colomer, J.,Gacia, E.,Soler, M.,Casamitjana, X., 2002. Effects of a turbid hydrothermal plume on the sedimentation rates in a karstic lake. Geophysical Research Letters 29, 2029.

Serra, T.,Soler, M., Julià, R.,Casamitjana, X.,Colomer, J., 2005. Behaviour and dynamics of a hydrothermal plume in Lake Banyoles, Catalonia, NE Spain. Sedimentology 52, 795–808.

Soler, M.,Serra, T.,Casamitjana, X.,Colomer, J., 2009. High sedimentation rates in a karstic lake associated with hydrothermal turbid plumes (Lake Banyoles, Catalonia, NE Spain). Sedimentary Geology 222, 5–15.

Stafford, K.W., Rosales-Lagarde, L., Boston, P.J., 2008a. Castile evaporite karst potential map of the Gypsum Plain, Eddy County, New Mexico and Culberson County, Texas: a GIS methodological comparison. Journal of Cave and karst Studies 70, 35-46.

Stafford, K.W., Nance, R., Rosales-Lagarde, L., Boston, P.J., 2008b. Epigene and hypogene gypsum karst manifestations of the Castile Formation: Eddy County, New Mexico and Culberson County, Texas, USA. International Journal of Speleology 37, 83-98.

Taheri, K., Gutiérrez, F., Mohseni, H., Raeisi, E., Taheri, M., 2015. Sinkhole susceptibility mapping using the analytical hierarchy process (AHP) and magnitude-frequency relationship: A case study in Hamadan province, Iran. Geomorphology 234, 64–79.

Teixell, A., Muñoz, J.A., 2000. Evolución tectonosedimentaria del Pirineo meridional durante el Terciario: una síntesis basada en la transversal del río Noguera Ribagorçana. Revista de la Sociedad Geológica de España 13, 251–264.

Trilla, J., Sanz, M., Pallí, L., 1979. Aplicación de un modelo de mezcla total en acuífero cárstico. In: Hidrogeología y recursos hidráulicos: II simposio nacional de hidrogeología: comunicaciones, Pamplona, 22-26 de octubre de 1979, vol. 4, p. 451-463.

Vergés, J., Millán, H., Roca, E., Muñoz, J.A., Marzo, M., Cirés, J., Den Bezemer, T., Zoetmeijer, R., Cloetingh, S., 1995. Eastern Pyrenees and related foreland basins:

pre-, syn- and post-collisional crustal scale cross-section. Mar. Petroleum Geol. 12, 893–915.

Vilanova, E., Menció, A., Mas-Pla, J., 2008. Determinación de sistemas de flujo regionales y locales en las depresiones tectónicas del Baix Empordà y La Selva (NE de España) en base a datos hidroquímicos e isotópicos. Boletín Geológico y Minero, 119(1), 51–62.

Vidal-Pardal, M., 1954. La alimentación subterránea del lago de Bañolas. Revista de Obras Públicas 102, tomo I (2869), pp. 223–227.

Vidal-Pardal, M., 1957. La alimentación subterránea del lago de Banyoles. Resultados de los ensayos con fluorescencia. Solución al problema de la regulación del Fluvià. Rev. Obr. Públ., año CV, nº 2903, p. 105–107, Madrid.

Vidal-Pardal, M., 1960. La alimentación subterránea del lago de Banyoles y algunos datos sobre los depósitos lacustres de sus inmediaciones. Min. Obr. Públ. Bol. nº 7. Serv. Geol. Infor. y Est. p. 23–40. Madrid.

Vigna, B., Fiorucci, A., Banzato, C., Forti, P., De Waele, J., 2010. Hypogene gypsum karst and sinkhole formation at Montcalvo (Asti, Italy). Zeitschrift für Geomorphology 54, 285–306.

Waltham, T., Bell, F., Culshaw, M., 2005. Sinkholes and subsidence. Springer, Dordrecht, 382 p.

Warren, J.K., 2016. Evaporites. A geological compendium. Springer, 1813 p.

Williams, P.W., 1972. The analysis of spatial characteristics of karst terrains. In: Chorley, R.J. (Ed.), Spatial Analysis in Geomorphology. Harper and Row, New York, pp. 135–163.

Xuewen, Z., Waltham, T., 2005. Tianken: Definition and description. Cave and Karst Science 32(2/3), 75–79.

Zarroca, M., Comas, X., Gutiérrez, F., Carbonel, D., Linares, R., Roqué, C., Mozafari, M., Guerrero, J., Pellicer, X.M., 2017. The application of GPR and ERI in combination with exposure logging and retrodeformation analysis to characterize sinkholes and reconstruct their impact on fluvial sedimentation. Earth Surf. Proc. Land. 42, 1049–1064.

Zarroca, M., Linares, R., Bach, J., Roque, C., Moreno, V., Font, Ll, Baixeras, C., 2012. Integrated geophysics and soil gas profiles as a tool to characterize active faults: the Amer fault example (Pyrenees, NE Spain). Environ. Earth. Sci. 67, 889–910.

Figure captions

Figure 1. General geological setting of the study area, located in the northern sector of the Ebro Cenozoic Basin, south of the Pyrenean Alpine orogene and west of the Neogene Emporda Graben. The rectangle indicates the area covered by the geological map of **figure 2**.

Figure 2. Geological map of the Garrotxa-Banyoles aquifer system, including the SMCV (based on Pallí and Trilla, 1979; Barnolas et al., 1994; Mató et al., 1996; Puig et al., 1997a, b, 2003; Martínez et al., 2000; Cirés et al., 2002; Carrillo, 2009; Gutiérrez et al., 2016).

Figure 3. Perpendicular geological cross-sections showing the complex stratigraphic and structural relationships of the Garrotxa-Banyoles artesian aquifer system. The trace of the sections is indicated in figure 2.

Figure 4. Stratigraphic section of SCMV. Data about the stratigraphic units underlying the Beuda Gypsum, including the carbonate aquifer of the Girona Fm., is known from boreholes.

Figure 5. Cartographic sketch and simplified cross-section showing the main features of the Garrotxa-Banyoles aquifer system and the distribution of epigene and hypogene gypsum karst settings. Inset images show aerial views of the Espolla overflow spring in dry conditions and Banyoles Lake with collapse structures in its bottom. Numbers indicate location of water sampling point of **table 1**.

Figure 6. Time series of monthly precipitation (Castellfollit de la Roca station) and piezometric data in the SMCV (gypsum aquifer; SMC) and the Espolla spring area; Fontcoberta-2 (F2) and -3 (F3) record hydraulic head in the gypsum aquifer and Fontcoberta-1 (F1) in the surficial tufaceous aquifer. Data from the Agència Catalana de l'Aigua.

Figure 7. Graphs showing ionic ratios in the different water sampling points. The waters in the discharge areas (purple ellipses) that have traversed the Beuda Gypsum through upward artesian flows show much higher Ca/HCO_3, and SO_4/HCO_3 ratios and Ca/SO_4 ratios close to one. Waters in the recharge area show the lowest SO_4/HCO_3 concentrations (red ellipse).

Figure 8. The stable isotope values (δ^2H and δ^{18}O) of the water samples collected in December 2016.

Figure 9. Geomorphological map of the SMCV including the cartographic sinkhole inventory. Inset rose diagram illustrates the frequency of the sinkhole orientations

constructed with the azimuth of the major axes of the 59 non-circular depressions, grouped into 12° classes (Georose 0.5.1 Software of Young Technology Inc, 2014).

Figure 10. Images of sinkholes of the SMCV. A: Large caprock collapse sinkhole with an ephemeral pond developed on a slope underlain by Banyoles Marls at the margin of the valley. B: Can Coromina caprock and cover collapse sinkhole. This circular depression, 80 m across, hosts a permanent pond and functions as a swallow hole. Arrow points to another collapse sinkhole. C: Pan-shaped sinkholes in a cop field. Most probably this is a collapse sinkhole whose scarped edges have been obliterated by human activity.

Figure 11. A, B: Sinkhole density models generated with a Kernel function and a search radius of 650 m. In A the density is based on the number of centroids and in B on the percentage area within sinkholes. C: N-S-oriented geological cross-section showing the variability of the number of sinkholes and their average diameter along the valley, computed for E-W bands 1 km wide. Note the higher number of sinkholes and their smaller size in the axial sector of the anticline, where the Banyoles Marls have been removed by erosion or have a limited thickness.

Figure 12. Graphs plotting cumulative frequency of sinkholes versus distance to the nearest neighbour. A: Graph constructed with all the sinkholes of the inventory; B: Graph constructed with the historical sinkholes on known age and the distance to the nearest pre-existing sinkhole. The major axis of the historical sinkholes is indicated.

Figure 13. A: Magnitude and frequency relationships constructed with the major axial length of the sinkholes inventoried in the SMCV (this work), the Fluvia Valley (Gutiérrez et al., 2016), Ambal salt pillow, Zagros Mountains (Gutiérrez and Lizaga, 2016), Hamedan, Zagros Mountains (Taheri et al., 2015), and Val D’Orleans, France (Gombert et al., 2015). B: Sketches showing the stratigraphy associated with the collapse sinkholes in the different areas and their relative scale.

Figure 14. A: Inverted resistivity image collected across a large caprock collapse sinkhole by a Dipole-Dipole array. B: Orthoimage showing the selected sinkhole within a sinkhole alignment and the trace of the ERI section. C: Oblique aerial view indicating the location of the ERI line.

Figure 15 Images of collapse mega-sinkholes related to hypogene karstification from different regions of the world (images A, B and D captured from Google Earth). A: Collapse sinkholes with lakes fed by underwater artesian springs in the Bottomless Lakes State Park, eastern margin of the Pecos River valley, New Mexico. Water rising from a confined limestone aquifer causes dissolution in the overlying evaporitic sediments, generating a monoclinal escarpment atop a dissolution front and a cluster of large sinkholes. B: Cluster of sinkholes (cenotes) of the Zacaton System, northeastern Mexico, attributed to the collapse of deep isolated chambers generated by hypogene limestone dissolution induced by rising CO_2 and H_sS gases of volcanic origin. El Zacatón is the second deepest underwater shaft in the world (>329 m). C: Kizoren Obruk in Central Anatolia, Turkey, a bedrock-collapse sinkhole 310 m across related to deep-seated dissolution of limestone by rising flows rich in carbon dioxide of magmatic origin. The bench corresponds to shelfstone-type bulbous tufa deposits, exposed by the recent lake level decline (ca. 20 m) due to groundwater withdrawal (Image taken in September 2015). D. Large caprock collapse sinkholes in the Interior Homocline of Saudi Arabia, generated by the hypogene karstification of the Hith anhydrite Formation and the collapse of the overlying formations. The sinkholes area associated with a monoclinal escarpment affected by extensional structures generated by the down-sip migration of a dissolution front in the Hith Formation.

	Name and number	Type of water point	Coordinates (UTM 31N / ETR S89) Elevation (m a.s.l.)	Litho.	Date of sample (references)	Cond (µS)	Tª (ºC)	pH	TDS (mg/l)	meq/l HCO_3^-	meq/l Cl^-	meq/l SO_4^{2-}	meq/l Ca^{2+}	meq/l Mg^{2+}	meq/l Na^+	meq/l K^+	% error (meq/l)	(meq/l) Na/Cl	(meq/l) Ca/SO_4^{2-}	(meq/l) Ca/HCO_3^-	(meq/l) SO_4/HCO_3	(meq/l) $Ca+Mg/HCO_3$	(meq/l) $Ca+Mg/HCO_3+SO_4$	SI Calcite	SI Gypsum	d18O (‰)	^{2}H (‰)
Recharge	Llierca **1**	River	390		04/1989 **(IGME, 1991)**				262	3	0.08	0.19	2.8	0.42	0.22	0.026		2.57	14.94	0.93	0.06	1.07	1.01			-7.8	
	Rocapastora **2**	Spring	477015/4677796 858	Carbonates	12/2016	560	10.7	8.51	516.22	5.773	0.123	0.657	6.075	0.243	0.117	0.023	-0.728	0.955	9.247	1.052	0.11	1.094	0.983	1.47	-1.87	-7.01	-44.6
					09/2017	514	12.1	8.02	436.37	4.879	0.172	0.533	4.99	0.23	0.19	0.001	-1.57	1.104	9.360	1.023	0.11	1.070	0.964				
	Falgars **3**	Spring	478256/4678475 750	Carbonates	12/2016	330	10.0	8.71	281.69	2.843	0.189	0.643	3.085	0.253	0.171	0.051	-1.587	0.906	4.8	1.085	0.23	1.174	0.958	1.12	-2.06	-6.66	-40.7
					09/2017	412	12.1	8.02	234.4	1.79	0.219	1.093	2.76	0.259	0.26	0.015	-3	1.185	2.525	1.542	0.61	1.687	1.047				
	Serradell **4**	Spring	468296/4681903 926	Carbonates	12/2016	360	11.2	8.40	303.12	3.243	0.094	0.572	3.440	0.221	0.093	0.022	-1.737	0.983	6.019	1.061	0.18	1.129	0.96	0.95	-2.08	-7.05	-47.8
					09/2017	Dry	Dry	Dry	Dry	Dry	Dry	Dry	Dry	Dry	Dry	Dry	Dry	Dry	Dry	Dry	Dry	Dry	Dry	Dry	Dry	Dry	Dry
Discharge (carbonate)	IRYDA **5**	Borehole	183 (400 deep)	Carbonates	1977-80 **(Sanz, 1985)**	1167	1			4.67		7.18									1.54						
	UABSA **6**	Borehole	479517/4664998 208.1 (340 deep)	Carbonates	**(Bach et al. 1986)**		17.0	7.2	834	5	0.6	6.3	9.02	1.01	0.5	0.038		0.83	1.43	1.8	1.26	2.01	0.89	1.671	1.44	-7.5 **(Sanz and Trilla, 1983)**	
					08/1989 **(IGME, 1991)**	618	18.0	7.17	795	4.21	0.34	6.6	8.3	2.58	0.48	0.026		1.41	1.26	197	1.56	2.58	1.01				
					06/2017 **(ACA, 2018)**		20.5	7.56		4.84			9.45	2.17						1.95		2.4	2.4				
Discharge (carbonate + gypsum)	Bullidors **7**	Overflow spring	473810/4664163 210.4	Carbonates + gypsum	09/1977-06/1979 **(Trilla et al. 1979)**	2532	19.3	6.3		5.11		25.74	31.15	1.42					1.21	6.09	5.04	6.37	1..6		**-0.03**		
					1977-80 **(Sanz, 1985)**	2560	19.0	7	2272.5	5.1	0.37	26.45	31.4	1.37	1.39	0.054		3.79	1.19	6.16	5.18	6.43	1.04		**-0.02**	-7.86 -7.7 **(Sanz and Trilla, 1983)**	
					04/1988 **(IGME, 1991)**				2391	5.21	1.27	28.11	27.5	5.16	1.43	0.845		1.13	0.98	5.28	5.39	6.27	0.98		**-0.08**		
	Montalt **8**	Sinkhole pond	479314/4662376 175	Carbonates + gypsum	12/2016	2204	13.1	8.67	2357.42	5.449	0.719	28.131	28.450	3.973	1.281	0.062	-0.782	1.781	1.011	5.221	5.16	5.951	0.966	1.95	**-0.05**	-6.78	-49.3
					09/2017	2550	21.8	7.06	2483.2	5.654	0.922	30.325	28.6	3.667	1.312	0.052	-4.64	1.423	0.943	5.058	5.36	5.707	0.897				
	Morgat **9**	Banyoles Lake (bucket V)	479496/4664435 172	Carbonates + gypsum	12/2016	1310	12.3	8.97	1126.69	3.374	0.536	12.326	12.680	2.885	0.860	0.048	0.726	1.606	1.029	3.758	3.65	4.613	0.991	1.78	**-0.54**	-5.74	-41
					09/2017	1437	23.8	7.78	1336.2	2.411	0.731	16.989	14.175	3.206	1.009	0.054	-4.37	1.381	0.834	5.879	7	7.209	0.896				
	Pudosa **10**	Spring	479573/4662157 176	Carbonates + gypsum	1977-80 **(Sanz, 1980)**	1712				6.72		13.12															
					(Bach et al. 1986)		16.0	7.0	1605.6	7.87	1.1	14	16.03	5.06	1.3	0.069		1.18	1.14	2.04	1.77	2.68	0.96				
					12/2016	1839	16.6	8.42	1677.86	5.904	0.708	17.595	17.95	4.598	1.344	0.064	-0.521	1.898	1.02	3.04	2.98	3.819	0.96	1.70	**-0.36**	-6.75	-47.7
					09/2017	Dry	Dry	Dry	Dry	Dry	Dry	Dry	Dry	Dry	Dry	Dry	Dry	Dry	Dry	Dry	Dry	Dry	Dry	Dry	Dry	Dry	Dry
Superficial shallow aquifers	Balca **11**	Sinkhole pond	473308/4663213 224	Marls	12/2016	940	7.1	7.73	804.06	5.631	1.802	3.078	5.790	1.180	1.509	2.153	0.576	0.837	1.881	1.028	0.55	1.238	0.8	0.59	-1.28	-5,06	-26
					09/2017	Dry	Dry	Dry	Dry	Dry	Dry	Dry	Dry	Dry	Dry	Dry	Dry	Dry	Dry	Dry	Dry	Dry	Dry	Dry	Dry	Dry	Dry
	Coromina **12**	Sinkhole pond	473719/4663066 225	Marls	12/2016	660	7.7	7.72	617.25	5.583	0.908	1.768	5.630	1.612	0.617	0.341	-0.356	0.68	3.185	1.008	0.32	1.297	0.985	0.60	-1.50	-2.19	-25.1
					09/2017	901	19.6	7.72	682.3	6.239	1.148	1.834	5.95	1.714	0.642	0.473	-2.45	0.559	3.245	0.954	0.29	1.229	0.949				
	Bertra **13**	Local spring	472411/4662063 289	Marls	12/2016	1040	9.0	8.02	958.93	7.349	2.11	3.875	8.17	4.750	1.034	0.138	2.764	0.49	2.108	1.112	0.53	1.758	1.151	1.29	-1.14	-5.89	-38.1
					09/2017	Dry	Dry	Dry	Dry	Dry	Dry	Dry	Dry	Dry	Dry	Dry	Dry	Dry	Dry	Dry	Dry	Dry	Dry	Dry	Dry	Dry	Dry
	Xervanda **14**	Spring	459122/4673837 318	Marls + volcanic rocks	12/2016	630	13.6	8.56	469.92	3.904	0.494	1.768	4.28	1.619	0.714	0.201	4.992	1.446	2.421	1.096	0.45	1.511	1.04	1.24	-1.61	-6.64	-48.2
					09/2017	693	14.3	7.20	487.3	4.112	0.604	1.719	4.37	1.628	0.797	0.186	4.07	1.32	2.543	1.063	0.42	1.459	1.029				

Table 1. Hydrochemical data from the sampling points grouped by different water types according to their position along the regional flow path. See location of points in figure 5. The associated bedrock lithology is indicated. Data from previous works are indicated by corresponding reference. Electrical conductivity, T and pH were measured in the field.

Highlights

Sinkholes related to hypogene gypsum dissolution

Caprock-collapse megasinkholes related to deep-seated interstratal dissolution

Frequency-size relationships of sinkholes in different contexts

Differences between sinkholes in epigene and hypogene settings

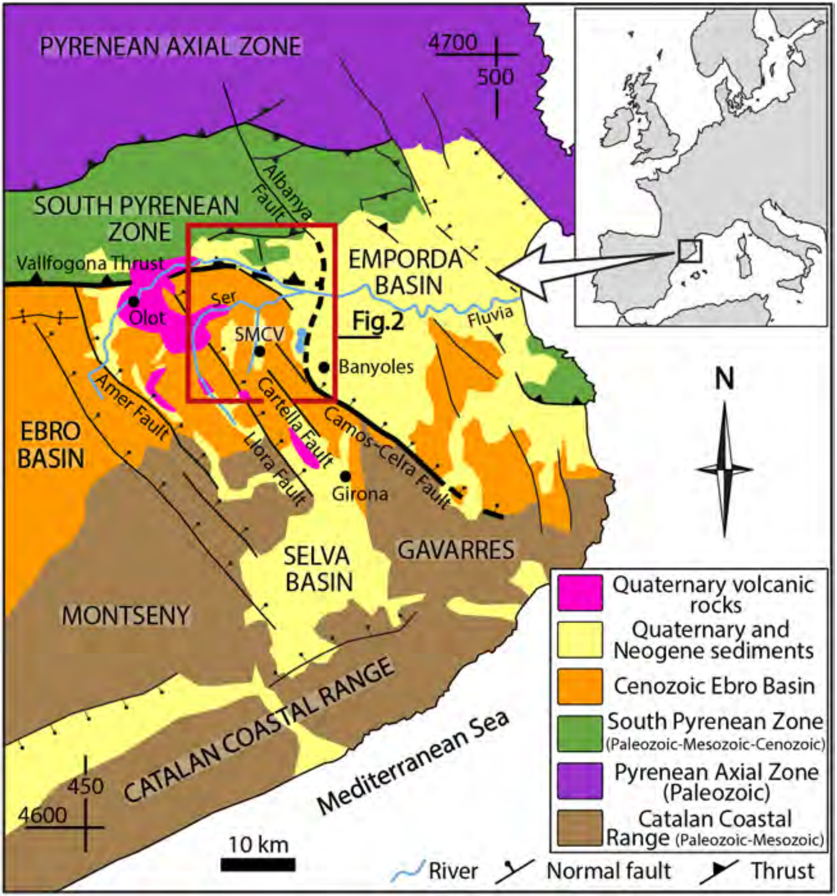
PYRENEAN AXIAL ZONE
4700
500
SOUTH PYRENEAN ZONE
Albanya Fault
Vallfogona Thrust
EMPORDA BASIN
Olot
Ser
SMCV
Fig.2
Fluvia
Banyoles
N
Amer Fault
Cartella Fault
Camos-Celra Fault
EBRO BASIN
Llora Fault
Girona
SELVA BASIN
GAVARRES
MONTSENY
CATALAN COASTAL RANGE
Mediterranean Sea
450
4600
10 km
Quaternary volcanic rocks
Quaternary and Neogene sediments
Cenozoic Ebro Basin
South Pyrenean Zone (Paleozoic-Mesozoic-Cenozoic)
Pyrenean Axial Zone (Paleozoic)
Catalan Coastal Range (Paleozoic-Mesozoic)
River
Normal fault
Thrust

Figure 1

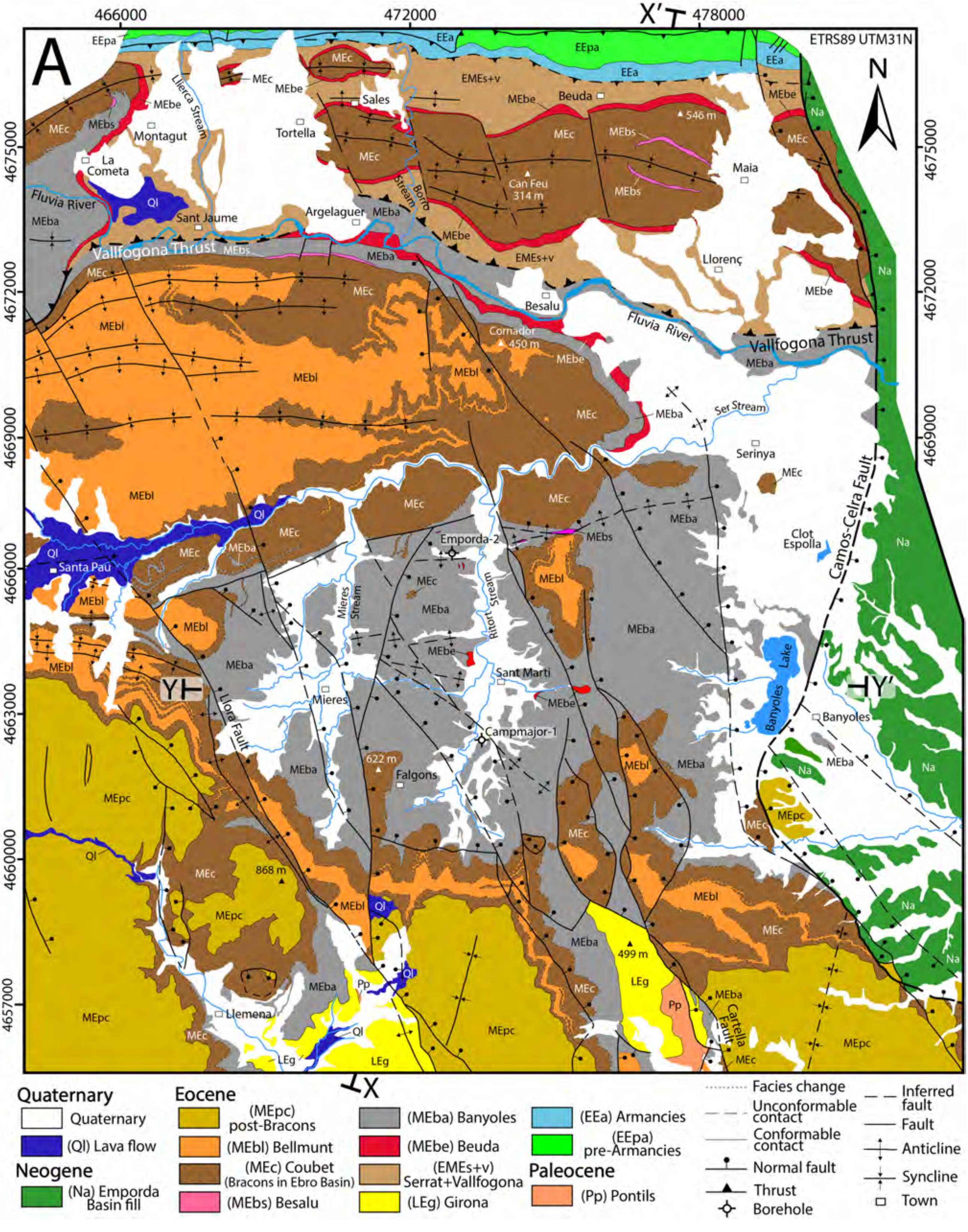

A
466000
472000
X'
478000
ETRS89 UTM31N
N
4675000
4672000
4669000
4666000
4663000
4660000
4657000
EEpa
EEa
MEc
MEbe
EMEs+v
Sales
Beuda
546 m
Llierca Stream
MEbs
Montagut
Tortella
La Cometa
Can Feu 314 m
Maia
Borro Stream
Fluvia River
Ql
Sant Jaume
Argelaguer
MEba
Vallfogona Thrust
Llorenç
Besalu
Na
Cornador 450 m
MEbl
Ser Stream
Serinya
Camos-Celra Fault
Clot Espolla
Emporda-2
Santa Pau
Mieres Stream
Ritort Stream
Sant Marti
Mieres
Y
Y'
Llora Fault
Campmajor-1
Lake Banyoles
Banyoles
622 m
Falgons
MEpc
868 m
499 m
LEg
Pp
Llemena
Cartella Fault
X
Quaternary
Quaternary
(Ql) Lava flow
Neogene
(Na) Emporda Basin fill
Eocene
(MEpc) post-Bracons
(MEbl) Bellmunt
(MEc) Coubet (Bracons in Ebro Basin)
(MEbs) Besalu
(MEba) Banyoles
(MEbe) Beuda
(EMEs+v) Serrat+Vallfogona
(LEg) Girona
(EEa) Armancies
(EEpa) pre-Armancies
Paleocene
(Pp) Pontils
Facies change
Unconformable contact
Conformable contact
Normal fault
Thrust
Borehole
Inferred fault
Fault
Anticline
Syncline
Town

Figure 2

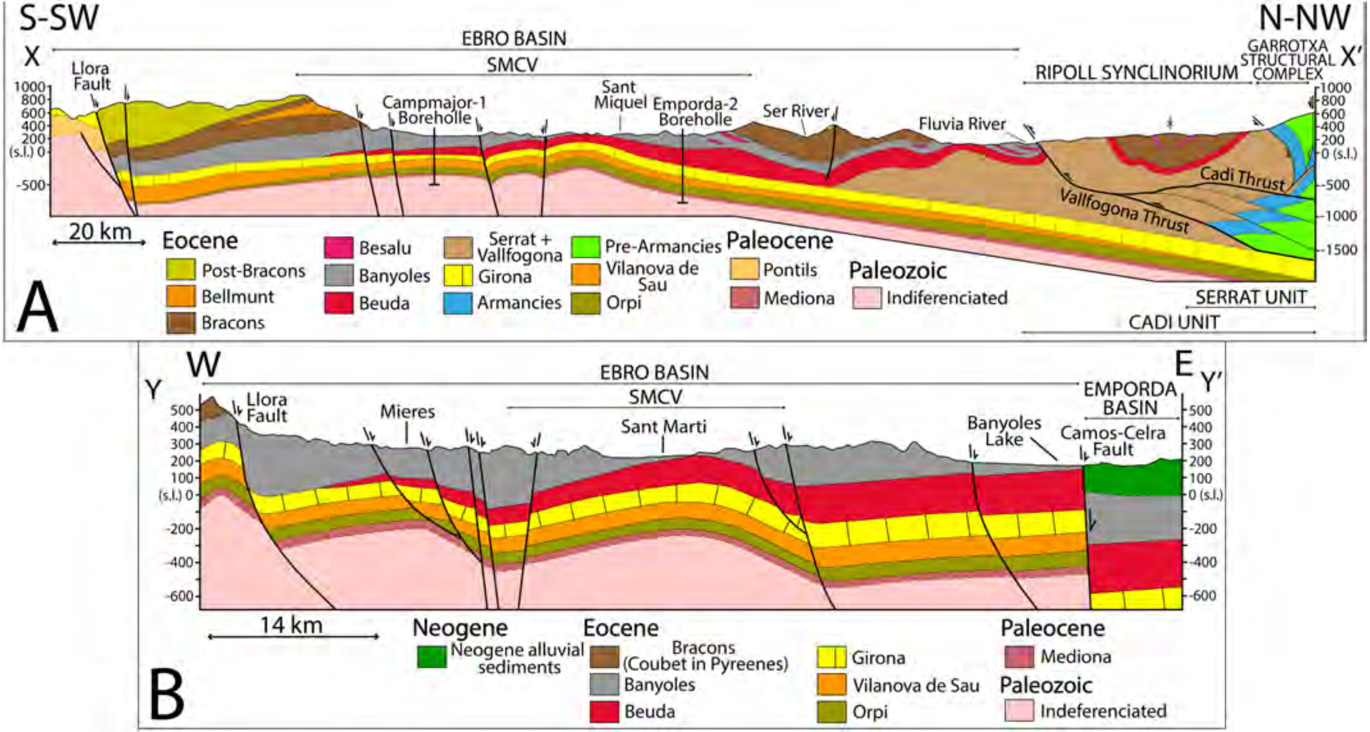
S-SW
N-NW
X
X'
EBRO BASIN
SMCV
RIPOLL SYNCLINORIUM
GARROTXA STRUCTURAL COMPLEX
Llora Fault
Campmajor-1 Borehole
Sant Miquel
Emporda-2 Borehole
Ser River
Fluvia River
Cadi Thrust
Vallfogona Thrust
1000
800
600
400
200
(s.l.) 0
-500
-1000
-1500
20 km
Eocene
Post-Bracons
Bellmunt
Bracons
Besalu
Banyoles
Beuda
Serrat + Vallfogona
Girona
Armancies
Pre-Armancies
Vilanova de Sau
Orpi
Paleocene
Pontils
Mediona
Paleozoic
Indiferenciated
SERRAT UNIT
CADI UNIT
A
W
E
Y
Y'
EBRO BASIN
SMCV
EMPORDA BASIN
Llora Fault
Mieres
Sant Marti
Banyoles Lake
Camos-Celra Fault
500
400
300
200
100
(s.l.) 0
-200
-400
-600
14 km
Neogene
Neogene alluvial sediments
Eocene
Bracons (Coubet in Pyreenes)
Banyoles
Beuda
Girona
Vilanova de Sau
Orpi
Paleocene
Mediona
Paleozoic
Indeferenciated
B

Figure 3

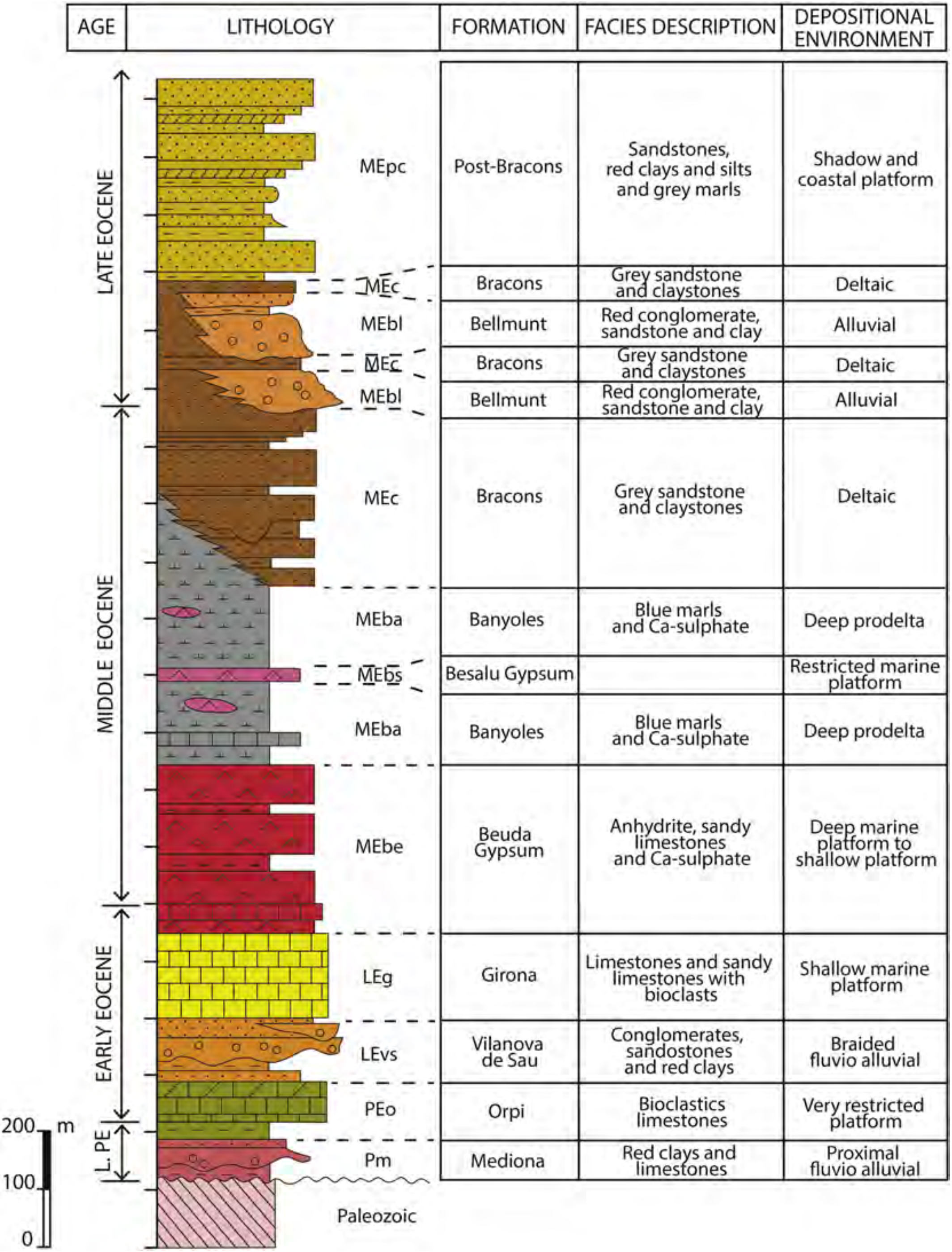

LITHOLOGY	FORMATION	FACIES DESCRIPTION	DEPOSITIONAL ENVIRONMENT
MEpc	Post-Bracons	Sandstones, red clays and silts and grey marls	Shadow and coastal platform
MEc	Bracons	Grey sandstone and claystones	Deltaic
MEbl	Bellmunt	Red conglomerate, sandstone and clay	Alluvial
MEc	Bracons	Grey sandstone and claystones	Deltaic
MEbl	Bellmunt	Red conglomerate, sandstone and clay	Alluvial
MEc	Bracons	Grey sandstone and claystones	Deltaic
MEba	Banyoles	Blue marls and Ca-sulphate	Deep prodelta
MEbs	Besalu Gypsum		Restricted marine platform
MEba	Banyoles	Blue marls and Ca-sulphate	Deep prodelta
MEbe	Beuda Gypsum	Anhydrite, sandy limestones and Ca-sulphate	Deep marine platform to shallow platform
LEg	Girona	Limestones and sandy limestones with bioclasts	Shallow marine platform
LEvs	Vilanova de Sau	Conglomerates, sandostones and red clays	Braided fluvio alluvial
PEo	Orpi	Bioclastics limestones	Very restricted platform
Pm	Mediona	Red clays and limestones	Proximal fluvio alluvial

Figure 4

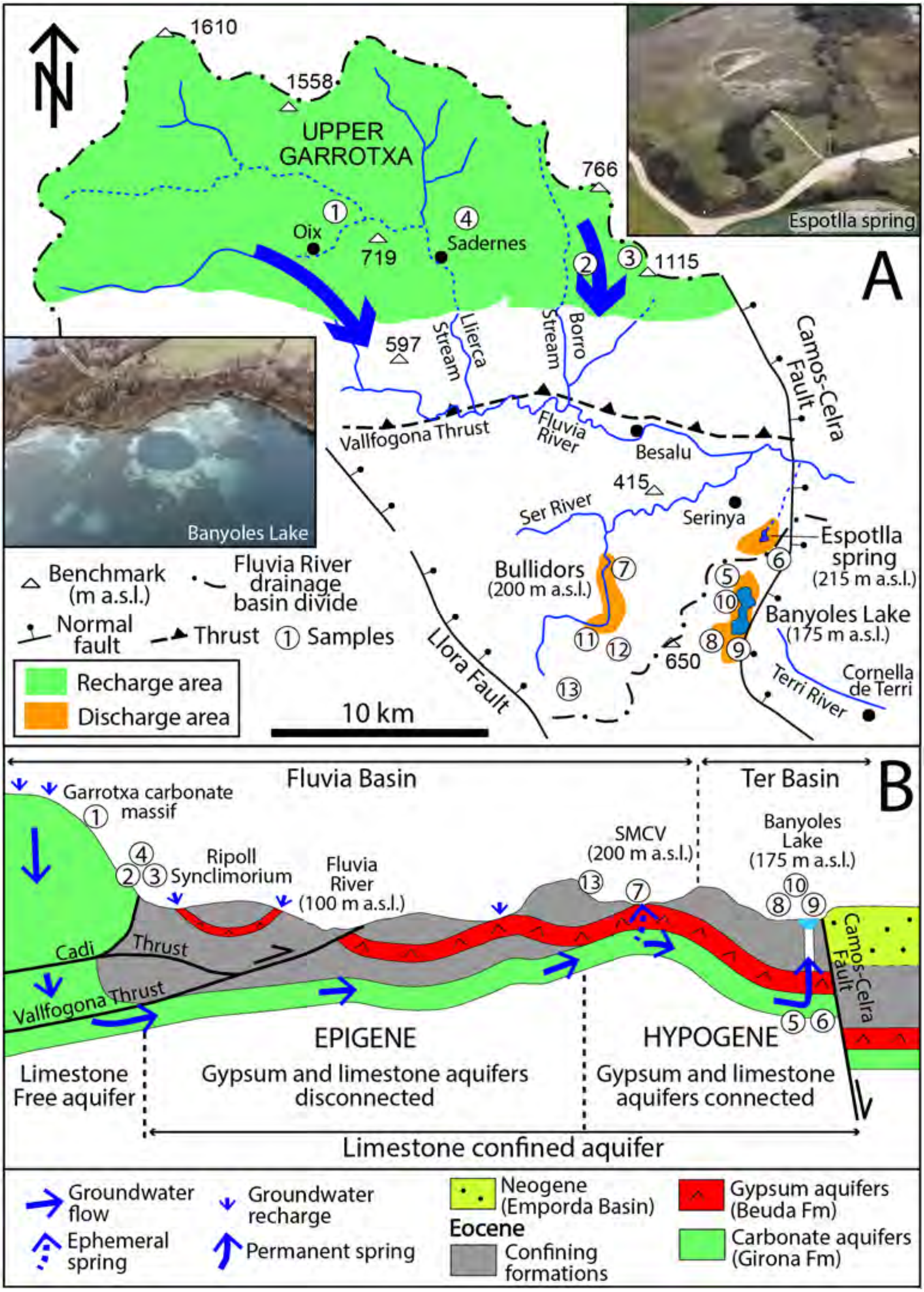
N
1610
1558
UPPER GARROTXA
766
1
Oix
719
4
Sadernes
2
3
1115
A
Espotlla spring
597
Llierca Stream
Borro Stream
Camos-Celra Fault
Vallfogona Thrust
Fluvia River
Besalu
415
Ser River
Serinya
Banyoles Lake
Espotlla spring (215 m a.s.l.)
6
5
10
Banyoles Lake (175 m a.s.l.)
Bullidors (200 m a.s.l.)
7
11
12
8
9
650
13
Llora Fault
Terri River
Cornella de Terri
Benchmark (m a.s.l.)
Fluvia River drainage basin divide
Normal fault
Thrust
1 Samples
Recharge area
Discharge area
10 km
Fluvia Basin
Ter Basin
B
Garrotxa carbonate massif
1
4
2 3
Ripoll Synclimorium
Fluvia River (100 m a.s.l.)
SMCV (200 m a.s.l.)
13
7
Banyoles Lake (175 m a.s.l.)
10
8 9
Cadi
Thrust
Vallfogona Thrust
Camos-Celra Fault
5 6
EPIGENE
HYPOGENE
Limestone Free aquifer
Gypsum and limestone aquifers disconnected
Gypsum and limestone aquifers connected
Limestone confined aquifer
Groundwater flow
Groundwater recharge
Ephemeral spring
Permanent spring
Neogene (Emporda Basin)
Eocene
Confining formations
Gypsum aquifers (Beuda Fm)
Carbonate aquifers (Girona Fm)

Figure 5

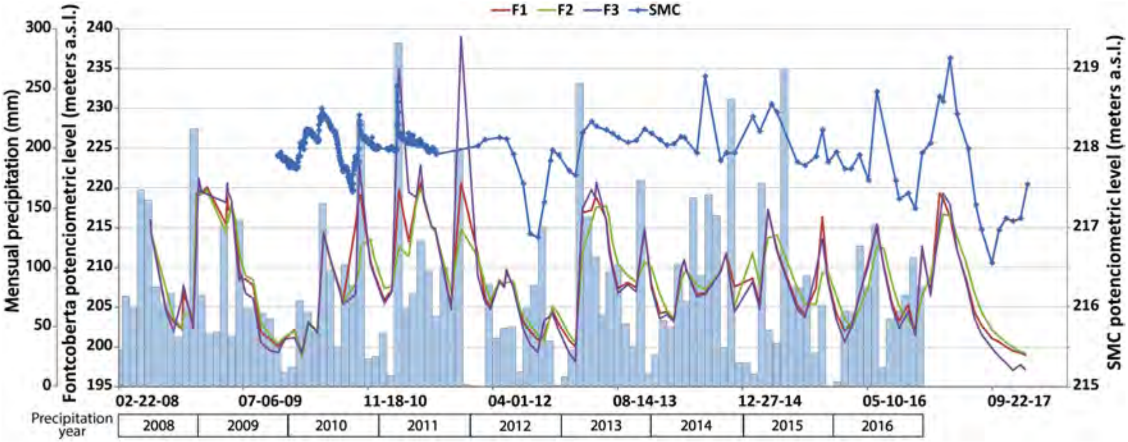
F1
F2
F3
SMC
Mensual precipitation (mm)
Fontcoberta potenciometric level (meters a.s.l.)
SMC potenciometric level (meters a.s.l.)
300
250
200
150
100
50
0
240
235
230
225
220
215
210
205
200
195
219
218
217
216
215
02-22-08
07-06-09
11-18-10
04-01-12
08-14-13
12-27-14
05-10-16
09-22-17
Precipitation year
2008
2009
2010
2011
2012
2013
2014
2015
2016

Figure 6

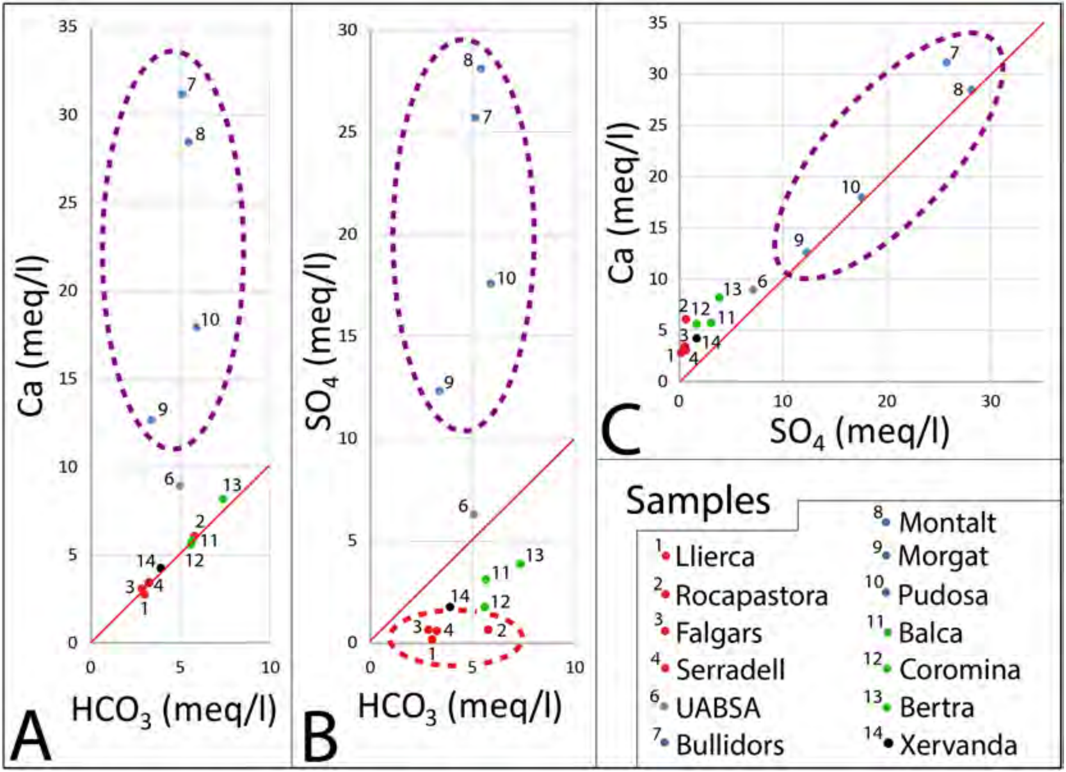
A
HCO$_3$ (meq/l)
Ca (meq/l)
0
5
10
15
20
25
30
35
0
5
10
1
2
3
4
6
7
8
9
10
11
12
13
14
B
HCO$_3$ (meq/l)
SO$_4$ (meq/l)
0
5
10
15
20
25
30
0
5
10
C
SO$_4$ (meq/l)
Ca (meq/l)
0
10
20
30
Samples
1 Llierca
2 Rocapastora
3 Falgars
4 Serradell
6 UABSA
7 Bullidors
8 Montalt
9 Morgat
10 Pudosa
11 Balca
12 Coromina
13 Bertra
14 Xervanda

Figure 7

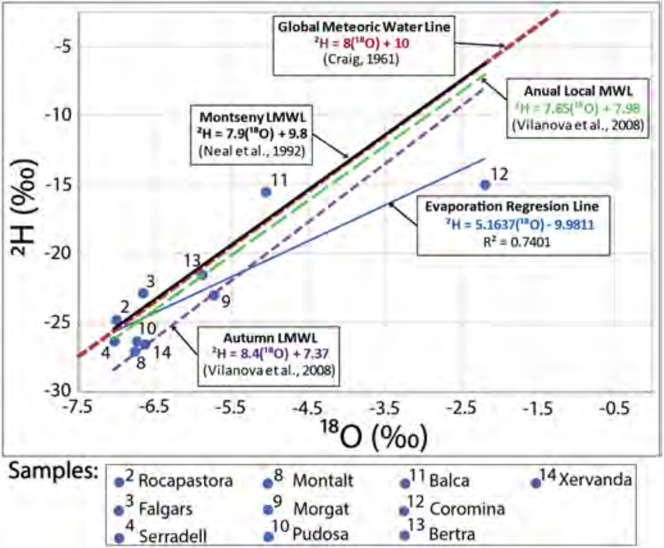
Global Meteoric Water Line
$^2H = 8(^{18}O) + 10$
(Craig, 1961)
Anual Local MWL
$^2H = 7.65(^{18}O) + 7.98$
(Vilanova et al., 2008)
Montseny LMWL
$^2H = 7.9(^{18}O) + 9.8$
(Neal et al., 1992)
Evaporation Regresion Line
$^2H = 5.1637(^{18}O) - 9.9811$
$R^2 = 0.7401$
Autumn LMWL
$^2H = 8.4(^{18}O) + 7.37$
(Vilanova et al., 2008)
11
12
13
3
9
2
10
4
14
8
-5
-10
-15
-20
-25
-30
-7.5
-6.5
-5.5
-4.5
-3.5
-2.5
-1.5
-0.5
^2H (‰)
^{18}O (‰)
Samples:
2 Rocapastora
3 Falgars
4 Serradell
8 Montalt
9 Morgat
10 Pudosa
11 Balca
12 Coromina
13 Bertra
14 Xervanda

Figure 8

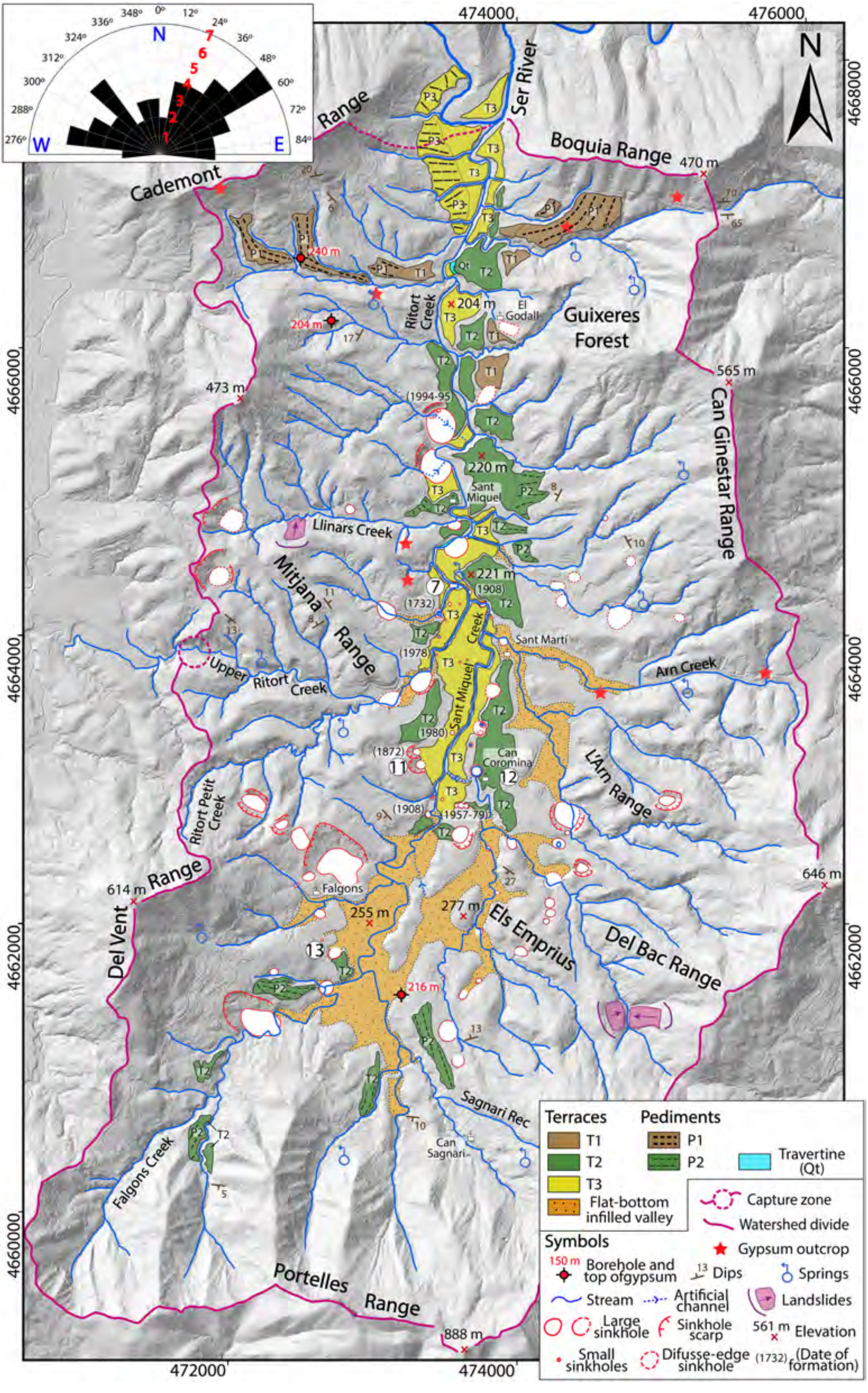

348º
0º
12º
24º
336º
324º
36º
312º
48º
300º
60º
288º
72º
276º
84º
N
W
E
1
2
3
4
5
6
7
474000
476000
4668000
4666000
4664000
4662000
4660000
472000
474000
N
Ser River
Range
Cademont
Boquia Range
470 m
P3
T3
P1
T1
Qt
T2
240 m
204 m
Ritort Creek
El Godall
Guixeres Forest
565 m
Can Ginestar Range
473 m
(1994-95)
220 m
Sant Miquel
P2
Llinars Creek
Mitjana Range
221 m
(1908)
(1732)
7
(1978)
Sant Martí
Arn Creek
Upper Ritort Creek
Sant Miquel Creek
(1980)
(1872)
11
Can Coromina
12
L'Arn Range
Ritort Petit Creek
(1908)
(1957-79)
Falgons
614 m
Range
Del Vent
646 m
255 m
277 m
Els Emprius
Del Bac Range
13
216 m
Sagnari Rec
Can Sagnari
Falgons Creek
Portelles Range
888 m
20
6
17
70
65
8
10
11
8
13
9
27
13
10
5
Terraces
T1
T2
T3
Flat-bottom infilled valley
Pediments
P1
P2
Travertine (Qt)
Capture zone
Watershed divide
Gypsum outcrop
Symbols
150 m Borehole and top ofgypsum
13 Dips
Springs
Stream
Artificial channel
Landslides
Large sinkhole
Sinkhole scarp
561 m Elevation
Small sinkholes
Difusse-edge sinkhole
(1732) (Date of formation)

Figure 9

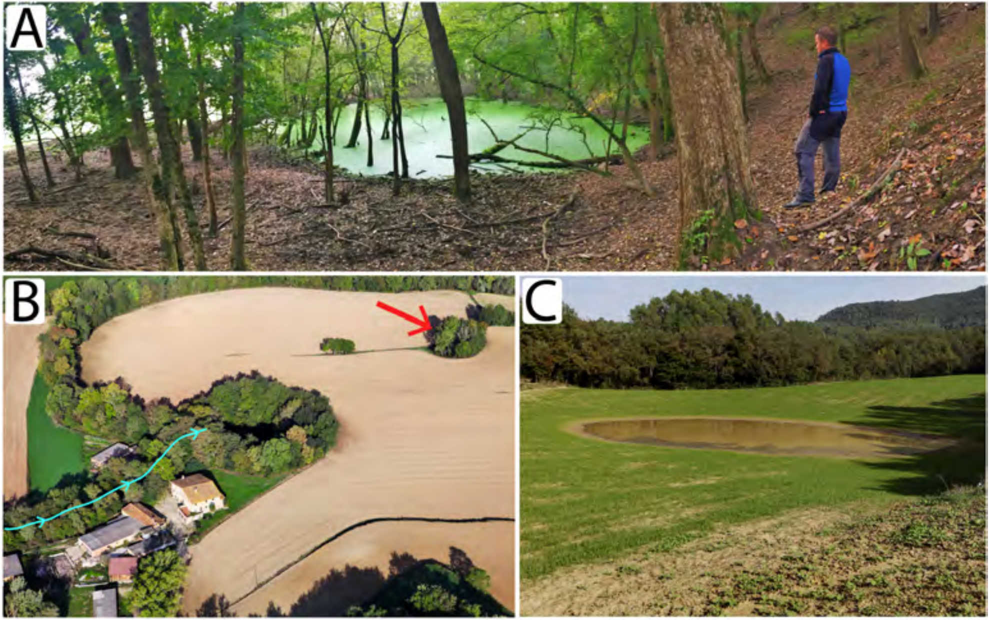

Figure 10

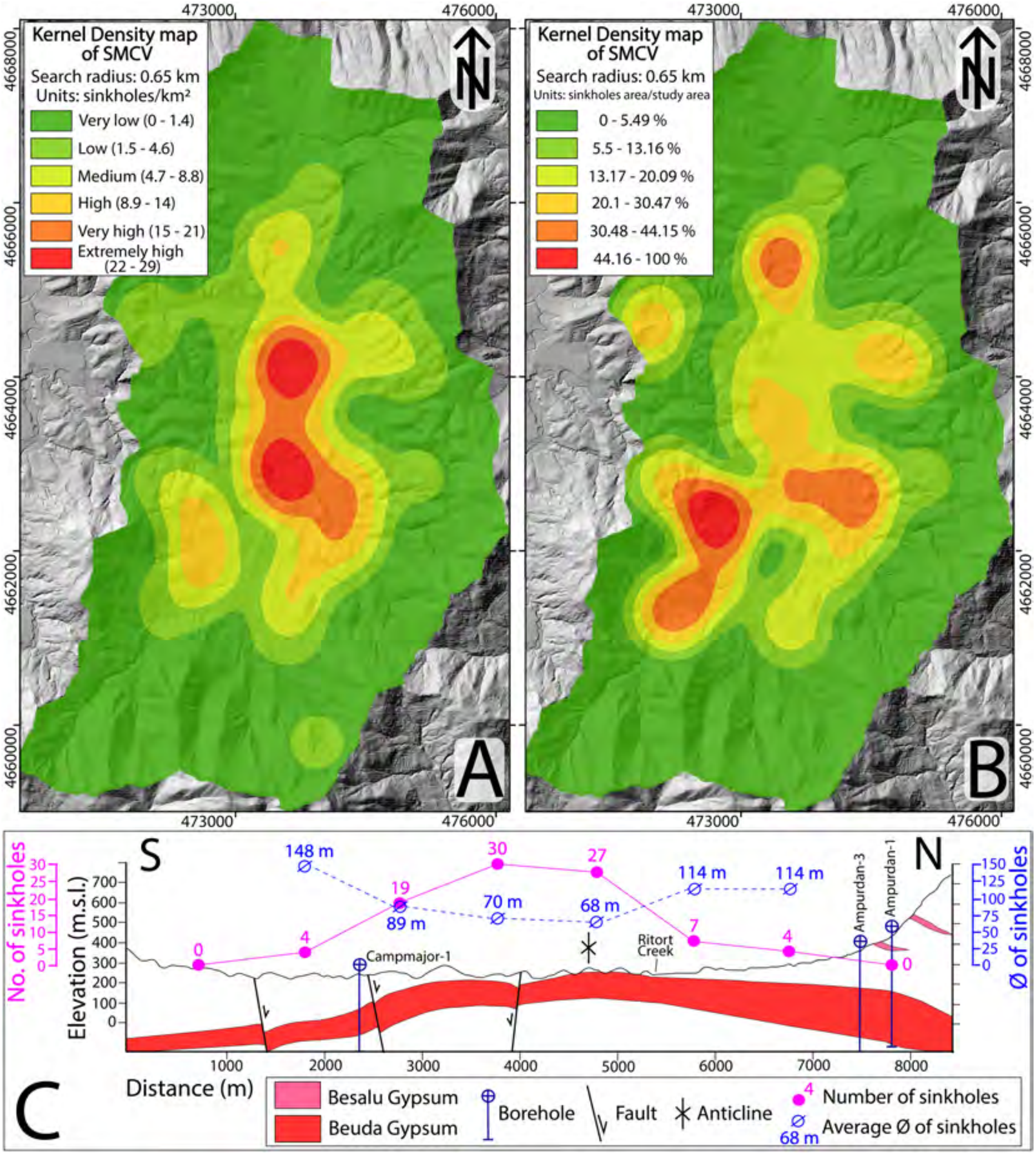
473000
476000
4668000
4666000
4664000
4662000
4660000
Kernel Density map of SMCV
Search radius: 0.65 km
Units: sinkholes/km²
🟩 Very low (0 - 1.4)
🟩 Low (1.5 - 4.6)
🟨 Medium (4.7 - 8.8)
🟨 High (8.9 - 14)
🟧 Very high (15 - 21)
🟥 Extremely high (22 - 29)
N
A
Kernel Density map of SMCV
Search radius: 0.65 km
Units: sinkholes area/study area
🟩 0 - 5.49 %
🟩 5.5 - 13.16 %
🟨 13.17 - 20.09 %
🟨 20.1 - 30.47 %
🟧 30.48 - 44.15 %
🟥 44.16 - 100 %
N
B
S
N
No. of sinkholes
0 5 10 15 20 25 30
Elevation (m.s.l.)
0 100 200 300 400 500 600 700
Ø of sinkholes
0 25 50 75 100 125 150
0
4
19
30
27
7
4
0
148 m
89 m
70 m
68 m
114 m
114 m
Campmajor-1
Ampurdan-3
Ampurdan-1
Ritort Creek
Distance (m)
1000 2000 3000 4000 5000 6000 7000 8000
C
Besalu Gypsum
Beuda Gypsum
Borehole
Fault
Anticline
4 Number of sinkholes
68 m Average Ø of sinkholes

Figure 11

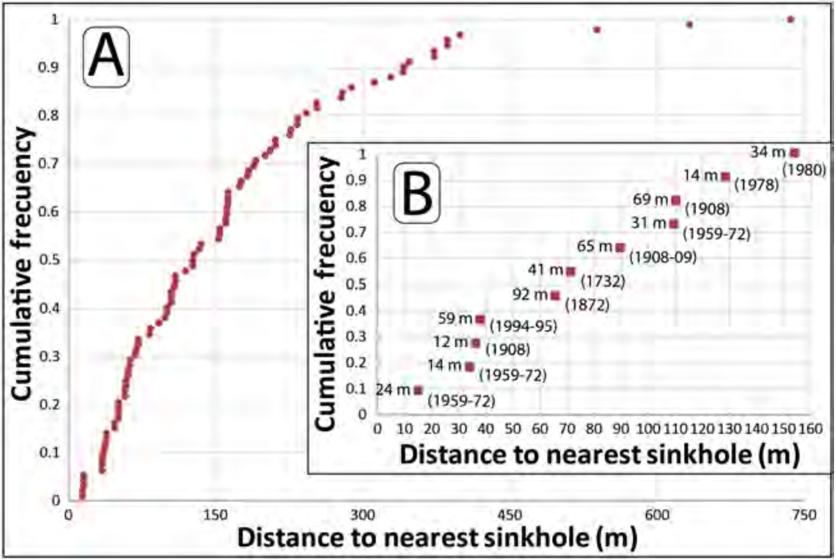
A
Cumulative frecuency
0
0.1
0.2
0.3
0.4
0.5
0.6
0.7
0.8
0.9
1
0
150
300
450
600
750
Distance to nearest sinkhole (m)
B
Cumulative frecuency
0
0.1
0.2
0.3
0.4
0.5
0.6
0.7
0.8
0.9
1
0
10
20
30
40
50
60
70
80
90
100
110
120
130
140
150
160
Distance to nearest sinkhole (m)
34 m (1980)
14 m (1978)
69 m (1908)
31 m (1959-72)
65 m (1908-09)
41 m (1732)
92 m (1872)
59 m (1994-95)
12 m (1908)
14 m (1959-72)
24 m (1959-72)

Figure 12

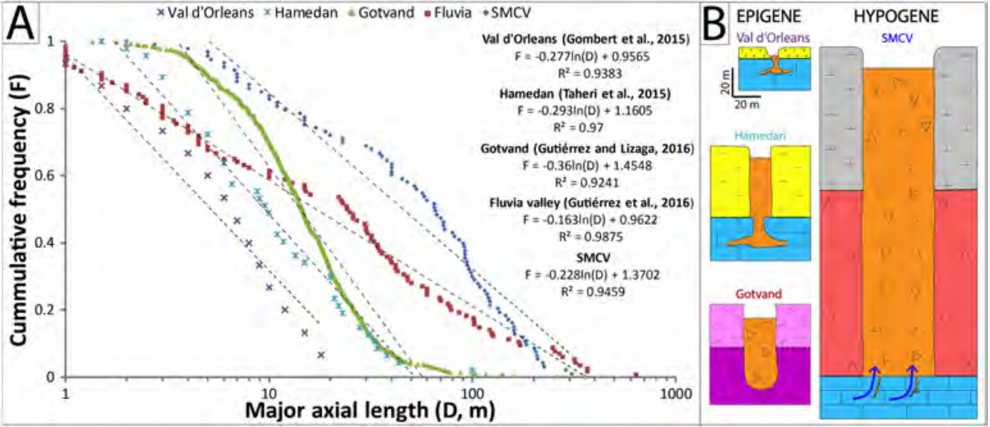
A
× Val d'Orleans
× Hamedan
▲ Gotvand
■ Fluvia
◆ SMCV
Val d'Orleans (Gombert et al., 2015)
F = -0.277ln(D) + 0.9565
R² = 0.9383
Hamedan (Taheri et al., 2015)
F = -0.293ln(D) + 1.1605
R² = 0.97
Gotvand (Gutiérrez and Lizaga, 2016)
F = -0.36ln(D) + 1.4548
R² = 0.9241
Fluvia valley (Gutiérrez et al., 2016)
F = -0.163ln(D) + 0.9622
R² = 0.9875
SMCV
F = -0.228ln(D) + 1.3702
R² = 0.9459
Cummulative frequency (F)
1
0.8
0.6
0.4
0.2
0
1
10
100
1000
Major axial length (D, m)
B
EPIGENE
HYPOGENE
Val d'Orleans
20 m
20 m
Hamedan
Gotvand
SMCV

Figure 13

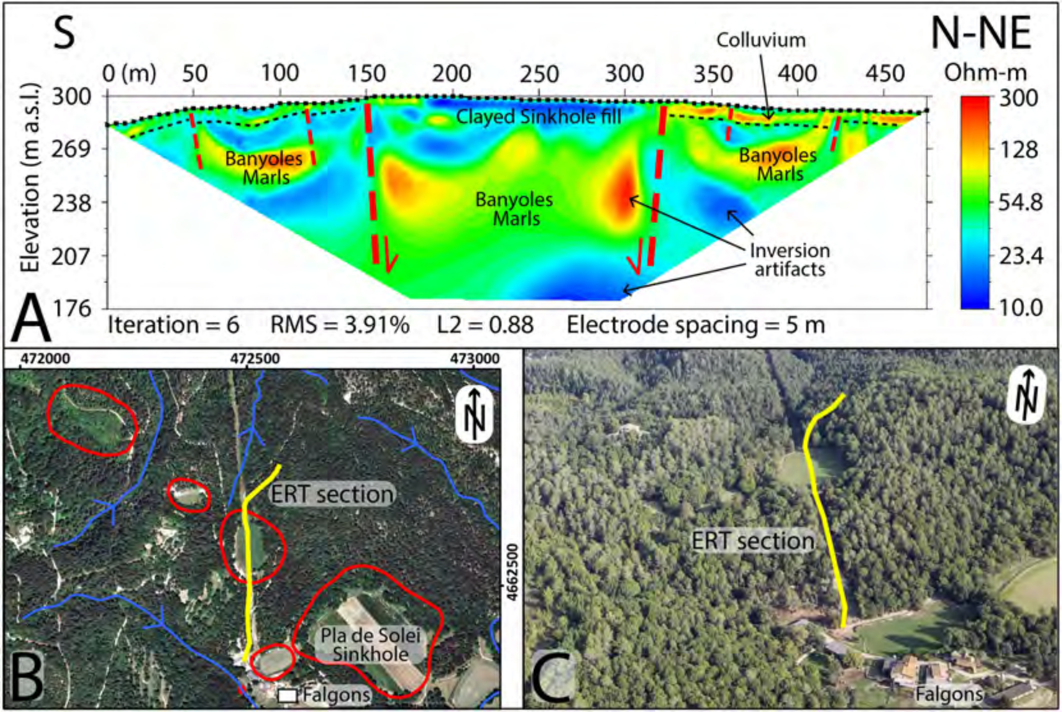
A
S
N-NE
0 (m)
50
100
150
200
250
300
350
400
450
Elevation (m a.s.l.)
300
269
238
207
176
Ohm-m
300
128
54.8
23.4
10.0
Colluvium
Clayed Sinkhole fill
Banyoles Marls
Banyoles Marls
Banyoles Marls
Inversion artifacts
Iteration = 6
RMS = 3.91%
L2 = 0.88
Electrode spacing = 5 m
B
472000
472500
473000
4662500
N
ERT section
Pla de Solei Sinkhole
Falgons
C
N
ERT section
Falgons

Figure 14

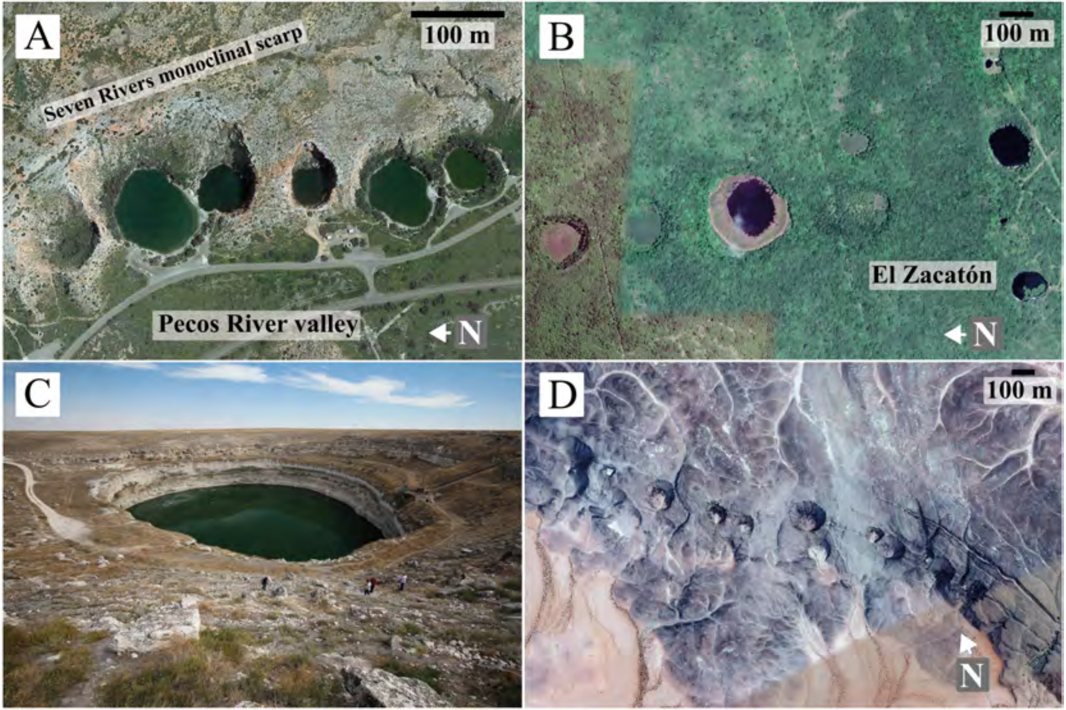
A
100 m
Seven Rivers monoclinal scarp
Pecos River valley
N
B
100 m
El Zacatón
N
C
D
100 m
N

Figure 15